

# A conservative interface-interaction method for compressible multi-material flows

Shucheng Pan, Luhui Han, Xiangyu Hu, Nikolaus. A. Adams

*Lehrstuhl für Aerodynamik und Strömungsmechanik, Technische Universität München, 85748 Garching, Germany*

---

## Abstract

In this paper we develop a conservative interface-interaction method dedicated to simulating multiple compressible fluids with sharp interface. Numerical models for finite-volume cells cut by more than two material-interface are proposed. First, we simplify the interface interaction inside such a cell to avoid the need for explicit interface reconstruction and very complex flux calculation. Second, conservation is strictly preserved by an efficient conservation correction procedure for the cut cell. To improve robustness, a multi-material scale separation model is developed to remove consistently non-resolved interface scales. In addition, a multi-resolution method and a local time-stepping scheme are incorporated into the proposed multi-material method to speed up high-resolution simulations. Various numerical test cases, including the multi-material shock tube problem, inertial confinement fusion implosion, triple-point shock interaction and shock interaction with multi-material bubbles, show that the method is suitable for a wide range of complex compressible multi-material flows.

*Keywords:* compressible multi-material flows, sharp interface method, multi-resolution simulations, level-set method, interface scale separation

---

## 1. Introduction

Compressible multi-material problems occur in a broad range of scientific and engineering areas such as high energy physics and astrophysics. Typical examples include in-

---

*Email addresses:* [shucheng.pan@tum.de](mailto:shucheng.pan@tum.de) (Shucheng Pan), [luhui.han@tum.de](mailto:luhui.han@tum.de) (Luhui Han), [xiangyu.hu@tum.de](mailto:xiangyu.hu@tum.de) (Xiangyu Hu), [nikolaus.adams@tum.de](mailto:nikolaus.adams@tum.de) (Nikolaus. A. Adams)

*Preprint submitted to Journal of Computational Physics*

*January 11, 2018*

ertial confinement fusion (ICF) [1], core-collapse supernova [2] and hypervelocity impact [3]. In these problems, different materials separated by the interface have significantly different material properties and equation of states (EOS). Large density or pressure jumps inside the material or across the interface may occur and may lead to complex flow fields and interface evolution. For such compressible multi-material problems, numerical modeling has received increasing attention in recent years due to its versatility as complement to experimental investigations. Many well-established methods have been proposed to simulate two-phase compressible flows, such as the front-tracking method [4], the arbitrary-Lagrangian-Eulerian (ALE) method [5], the volume-of-fluid (VOF) [6] and the level-set method [7]. Among these, sharp interface methods have the advantage of introducing no numerical mixing artifacts due to the interface model for immiscible materials or shock-driven miscible materials.

Unlike front-tracking and ALE methods, VOF and level-set methods can avoid the problem of capturing complex geometries of interfaces as they implicitly define the interface and solve its evolution. Although VOF inherently is conservative, it treats the interface with a smeared interface representation which is disadvantageous for immiscible materials problems or extremely fast high energy processes. When more than two materials are involved, complex interface reconstruction algorithms, such as onion-skin [8] and serial-dissection [9], are needed to generate interface locations from the volume-fraction data, usually relying on a material ordering strategy. The mixed treatment for fluid states inside a cell occupied by more than two materials (hereafter referred to as multi-material-cell) in the VOF method does not ensure a sharp-interface representation [10]. In the level-set method, the interface reconstruction is straightforward via a signed distance function as the interface implicitly is represented by the zero contour which can be considered as a non-smeared interface representation. The sharp-interface property can be imposed by interface-interaction treatment [11] for two-phase flows. For multi-material flows involving more than two fluids, problems arise when the interface-network motion needs to be captured and interface interaction occurs inside a multi-material-cell. The former issue can be addressed by a recently developed multi-region level-set method [12] which offers higher computational efficiency than the multiple level-set method [13] and better accuracy than the regional level-set method [14]. The latter issue can be



handled by applying the ghost fluid method [15] on the multiple level-set functions to avoid complex interface interaction. This, however, leads to violation of conservation [16, 13]. Conservative interface interaction models have been developed for two-phase flows [17, 18], but, to our knowledge, have not yet been proposed for more than two fluids.

Numerical methods may suffer from a lack of robustness when complex interface topology changes, such as sudden generation and destruction of thin filaments and isolated droplets, are encountered. Interface scale separation models based on the refined level-set method [19, 20] and identifying resolved/non-resolved interface segments [21] have been proposed for two-phase flows to remove non-resolved structures. More recently a model employing the constrained stimulus-response procedure [22, 23] has been developed for interface scale separation and increases the robustness for the simulations of compressible interfacial flows. However, scale separation for more than two materials has not been presented in the literature, and the extension of previous models [19, 20, 22, 23] is not straightforward.

The objective of the present paper is to develop an efficient and robust numerical method for compressible multi-material flows. In order to ensure conservation and the sharp-interface property, several operations related to the interface network are proposed. First, the interface-network evolution is captured accurately and efficiently by a multi-region level-set method, which is a combination of the original level-set method and the regional level-set method, to adopt the respective advantages of these two methods. In order to maintain conservation and impose a sharp-interface treatment, we extend the two-phase conservative sharp-interface method by introducing a conservation correction and a reduced interface-interaction model in each multi-material-cell. A multi-material interface scale separation model is proposed to remove non-resolved interface segments and thus to increase the robustness of high-resolution low numerical dissipation simulations. The paper is structured as follows. In Sec. 2, the multi-material sharp-interface method, including the multi-region level-set method, conservative finite volume method, reduced interface-interaction model and multi-material interface scale separation operation, is detailed. The proposed method gains computational efficiency by the employed multi-resolution method and a local time-stepping scheme. The accuracy, capability and

robustness of the method are demonstrated in Sec. 3 by a range of numerical examples, followed by a concluding remark.

## 2. Numerical method

### 2.1. Governing equations

The governing equations of inviscid compressible flows are

$$\frac{\partial \mathbf{U}}{\partial t} + \nabla \cdot \mathbf{F}(\mathbf{U}) = 0, \quad (1)$$

where  $\mathbf{U} = (\rho, \rho u, \rho v, \rho w, \rho E)^T$ , in which  $\rho$ ,  $u$ ,  $v$ ,  $w$ , and  $\rho E$  are the density, the three velocity components and the total energy with relation  $E = e + \frac{1}{2}(u^2 + v^2 + w^2)$ , with  $e$  being the internal energy per unit mass. The inviscid flux tensor  $\mathbf{F}$  is

$$\mathbf{F}(\mathbf{U}) = \begin{bmatrix} \rho u & \rho v & \rho w \\ \rho u^2 + p & \rho v u & \rho w u \\ \rho u v & \rho v^2 + p & \rho w v \\ \rho u w & \rho v w & \rho w^2 + p \\ u(\rho E + p) & v(\rho E + p) & w(\rho E + p) \end{bmatrix}. \quad (2)$$

To close the governing equations EOS is required to describe the thermodynamic properties of the materials. The EOS for an idea gas is

$$p = (\gamma - 1)\rho e, \quad (3)$$

where  $\gamma$  is the ratio of specific heats. For water-like fluids, the pressure can be determined by Tait's equation of state

$$p = B \left( \frac{\rho}{\rho_0} \right)^\gamma - B + p_0, \quad (4)$$

where  $\rho_0$  and  $p_0$  are the reference density and pressure, and  $B$  is a constant. Other EOS may also be employed in compressible multi-material flows, such as the stiffened gas EOS for water under very high pressure, the Jones-Wilkins-Lee (JWL) EOS for gaseous detonation-products and the Mie-Grüneisen (MG) EOS for solids [24].

Multi-material fluid dynamic problems contain multiple different fluids. We assume that there are  $\mathcal{N}$  materials (or fluids) in the problem and partition the entire domain,  $\Omega = \bigcup_{\chi \in \mathbf{X}} \Omega^\chi$ , where  $\Omega^\chi$  is the material domain and  $\mathbf{X} = \{\chi \in \mathbb{N} | 1 \leq \chi \leq \mathcal{N}\}$  is the index

set for all materials. Given  $\xi, \eta \in \mathbf{X}$  and  $\xi \neq \eta$ , we define  $\partial\Omega^\xi$  as the material boundary,  $\Gamma_{\xi\eta} = \partial\Omega^\xi \cap \partial\Omega^\eta$  as the pairwise material interface that separates two material domains,  $\Gamma = \bigcup \Gamma_{\xi\eta}$  as the interface network, and  $\mathbf{J} = \bigcap \Gamma_{\xi\eta}$  as multiple junctions. Each material has its individual material parameters (e.g. [viscosity](#)) and EOS.

## 2.2. Interface capturing

To capture the evolution of complex interface networks, we have developed the multi-region level-set method which is a combination of the original level-set method [7] and the regional level-set method [14]. Globally we use a single regional level-set for representing the multi-region (or multi-material) system to significantly reduce the memory cost. Locally we construct multiple local level-set functions to capture directly the evolution of the interface network in order to save computational effort and avoid inaccuracies in reconstructing the interface network. Although the total number of materials may be very large, locally the number is limited, such that solving multiple locally constructed level-set advection equations is efficient. This method has demonstrated to achieve high-order accuracy for typical test cases without generation of artifacts[12].

The total system can be represented by the regional level-set function  $\varphi^\chi(\mathbf{x}) = (\varphi(\mathbf{x}), \chi(\mathbf{x}))$ , where  $\varphi(\mathbf{x}) \geq 0$  is the unsigned distance function and  $\chi(\mathbf{x})$  is an integer material indicator. The material domain  $\Omega^a$  is identified by the indicator,  $\Omega^\xi = \{\mathbf{x} | \chi(\mathbf{x}) = \xi\}$ , and the interface network is defined as  $\Gamma = \{\mathbf{x} | \varphi(\mathbf{x}) = 0\}$ . On a two-dimensional uniform Cartesian grid, the regional level-set  $\varphi_{i,j}^\chi = (\varphi_{i,j}, \chi_{i,j})$  is defined at the center of the finite-volume cell  $C_{i,j}$ . The  $\mathcal{N}_s$  materials contained in a local set of cells

$$V_s = \{C_{k,l} | i-1 < k < i+1, j-1 < l < j+1\} \quad (5)$$

are identified by a local index set  $\mathbf{X}_s = \{r \in \mathbb{N} | 1 \leq r \leq \mathcal{N}_s\}$ .

By using a construction operator for generating the local multiple level-set fields and a reconstruction operator for reconstructing the global regional level-set field from the local level-set fields, the evolution step contains three main operations for  $C_{i,j}$ :

- (1) Construct  $\mathcal{N}_s$  local level-set fields  $\phi_{k,l}^{r,n}$  for the current time-step  $n$  at the center of

each cell  $C_{k,l}$  which belongs to the spatial discretization stencil of  $C_{i,j}$ :

$$\phi_{k,l}^{r,n} = \mathbf{C}_r \left( \varphi_{k,l}^\chi \right) = \begin{cases} \varphi_{k,l} & \text{if } \chi_{k,l} = \chi_r \\ -\varphi_{k,l} & \text{otherwise} \end{cases}, \quad r \in \mathbf{X}_s \quad (6)$$

(2) Compute the updated  $\phi_{i,j}^{r,n+1}$  at the next time-step  $n+1$  by solving  $\mathcal{N}_s$  local advection equations. The formulation of the local advection equation depends on  $\mathcal{N}_s$ . If  $\mathcal{N}_s \leq 2$  it recovers the original level-set advection equation while if  $\mathcal{N}_s \geq 3$  it can be rewritten as

$$\begin{aligned} \phi_{i,j}^{r,(s+1)} &= \beta_p \phi_{i,j}^{r,n} + (1 - \beta_p) \left[ \phi_{i,j}^{r,(s)} - \Delta t \mathbf{v}_{i,j}^n \cdot (\nabla \phi^r)_{i,j}^{(p)} \right], \quad 0 \leq p \leq m, r \in \mathbf{X}_s, \\ \phi_{i,j}^{r,(0)} &= \phi_{i,j}^{r,n}, \quad \phi_{i,j}^{r,(m+1)} = \phi_{i,j}^{r,n+1}, \end{aligned} \quad (7)$$

where  $m$  is the number of Runge-Kutta sub-steps,  $\beta_p$  is the parameter in the  $p$ -th sub-step,  $\mathbf{v}$  is the advection velocity, and  $(\nabla \phi^r)_{i,j}^{(p)}$  is the finite difference approximation of the spatial derivative at the center of a finite-volume cell  $C_{i,j}$ .

(3) Reconstruct the new regional level-set  $\varphi_{i,j}^\chi$  at the center of  $C_{i,j}$  from the  $\mathcal{N}_s$  new local level-set fields  $\phi_{i,j}^{r,n+1}$  by the reconstruction operator  $\mathbf{R}$  as

$$\varphi_{i,j}^\chi = \mathbf{R} \left( \phi_{i,j}^{r,n+1}, r \in \mathbf{X}_s \right) = \left( \left| \max_{i,j} \phi_{i,j}^{r,n+1} \right|, \arg \max_{\chi_r} \phi_{i,j}^{r,n+1} \right). \quad (8)$$

We consider a 1D two-region case in Fig. 1 to illustrate the interface capturing scheme above. Suppose we have the regional level-set function  $\varphi^{\chi,n}$  (solid line in Fig. 1(a)) at time step  $n$ , and we want to obtain  $\varphi^{\chi,n+1}$  (dashed line in Fig. 1(a)). The velocity field  $u$  is set as constant for simplicity. Following the algorithm above, first we use the construction operator to construct the local level-set functions. For instance, as the local index set of the cut-cell  $i = 6$  is  $\mathbf{X}_s = \{1, 2\}$ , the two local level-set functions defined on the stencil of cell  $i = 6$ ,  $\phi^{1,n}$ ,  $\phi^{2,n}$ , are shown in Fig. 1(b). We use Eq. (7) to advect these local level-sets,

$$\phi_{i=6}^{1,n+1} = \phi_{i=6}^{1,n} + \Delta t u \left( \frac{\partial \phi^1}{\partial x} \right)_{i=6}^n, \quad \phi_{i=6}^{2,n+1} = \phi_{i=6}^{2,n} + \Delta t u \left( \frac{\partial \phi^2}{\partial x} \right)_{i=6}^n, \quad (9)$$

where for simplicity an explicit Euler time marching is used for illustration. The numerical approximation of  $\left( \frac{\partial \phi^1}{\partial x} \right)^n$  depends on the specific spatial discretization scheme. The updated values for cell  $i = 6$ ,  $\phi_{i=6}^{1,n+1}$  and  $\phi_{i=6}^{2,n+1}$ , are plotted in Fig. 1(b). Applying the reconstruction operator gives

$$\varphi_{i=6}^\chi = \mathbf{R} \left( \phi_{i=6}^{1,n+1}, \phi_{i=6}^{2,n+1} \right) = \left( \left| \phi_{i=6}^{1,n+1} \right|, 1 \right), \quad (10)$$

which indicates that cell  $i = 6$  does not change its material indicator. For cell  $i = 7$  one has

$$\varphi_{i=7}^x = \left( \left| \phi_{i=7}^{1,n+1} \right|, 1 \right) \quad (11)$$

which corresponds to an indicator change from  $\chi_{i=7}^n = 2$  to  $\chi_{i=7}^{n+1} = 1$ . For more complex 2D examples involving multiple junctions we refer to Ref. [12].

### 2.3. Conservative sharp-interface method

We extend the two-phase discretized governing equation of the conservative sharp-interface method [18] to multiple materials. On a two-dimensional uniform Cartesian grid with grid spacings  $\Delta x$  and  $\Delta y$ , the flow variable  $\mathbf{U}$  is defined at the center of each finite-volume cell. For each material  $\chi$  residing in cell  $C_{i,j}$ , we can integrate Eq. 2 over the space-time volume  $C_{i,j} \cap \Omega^\chi(t)$  and apply the Gauss theorem to obtain

$$\int_n^{n+1} dt \int_{\alpha_{i,j}^\chi(t)} dx dy \frac{\partial \mathbf{U}}{\partial t} + \int_n^{n+1} dt \int_{\partial C_{i,j} \cap \Omega^\chi(t)} dx dy \mathbf{F} \cdot \mathbf{n} = 0, \quad (12)$$

where  $\alpha_{i,j}^\chi(t)$  is the time dependent volume fraction of material  $\chi$  in  $C_{i,j}$ .  $\partial C_{i,j} \cap \Omega^\chi(t)$  contains two parts: one is the combination of the four segments of the cell faces after being cut by the material interface, which can be written in the form of  $A_{i+1/2,j}^\chi(t)\Delta y$ ,  $A_{i,j+1/2}^\chi(t)\Delta x$ ,  $A_{i-1/2,j}^\chi(t)\Delta y$ , and  $A_{i,j-1/2}^\chi(t)\Delta x$ , where  $A^\chi(t)$  is the aperture, see Fig. 3(a); the other one, denoted as  $\Delta\Omega_{i,j}^\chi$ , is the segment of material boundary  $\partial\Omega^\chi$  inside cell  $C_{i,j}$ . This integral equation can be discretized with an explicit Euler time marching scheme as

$$\begin{aligned} \alpha_{i,j}^{\chi,n+1} \mathbf{U}_{i,j}^{n+1} &= \alpha_{i,j}^{\chi,n} \mathbf{U}_{i,j}^n + \frac{\Delta t}{\Delta x} \left[ A_{i-1/2,j}^\chi \hat{\mathbf{F}}_{i-1/2,j} - A_{i+1/2,j}^\chi \hat{\mathbf{F}}_{i+1/2,j} \right] \\ &+ \frac{\Delta t}{\Delta x} \left[ A_{i,j-1/2}^\chi \hat{\mathbf{F}}_{i,j-1/2} - A_{i,j+1/2}^\chi \hat{\mathbf{F}}_{i,j+1/2} \right] + \frac{\Delta t}{\Delta x \Delta y} \hat{\mathbf{X}}(\Delta\Omega_{i,j}^\chi), \end{aligned} \quad (13)$$

where  $\Delta t$  is the time step size determined by CFL condition.  $\alpha_{i,j}^\chi \mathbf{U}_{i,j}$  is the conservative quantity vector in  $C_{i,j}$ , with  $\mathbf{U}_{i,j}$  being the cell-averaged quantity vector of the material  $\chi$ .  $\hat{\mathbf{F}}$  is the numerical flux at cell-face and  $\hat{\mathbf{X}}(\Delta\Omega_{i,j}^\chi)$  is the momentum and energy exchange flux determined by the interface interaction model discussed in Sec. 2.3.3. For Runge-Kutta time discretization, Eq. (13) is synonymous for a substep.

To update of the volume fraction from the regional level-set function, we use the algorithm in Ref. [25]. Suppose we want to compute the volume fraction  $\alpha_r$  of a particular

material  $r$  in a cut-cell with  $\mathcal{N}_s$  materials. This algorithm, as in Ref. [26], recursively subdivides a cut-cell into 4 (8 in 3D) sub-cells with equal size. The volume fraction of each sub-cell  $\alpha_s$  is determined by the sign of its local level-set  $\phi^r$  at vertices (obtained by the bilinear/trilinear interpolation), i.e.,  $\alpha_s = 1$  for full sub-cells (all vertex level-set values are positive),  $\alpha_s = 0$  for empty sub-cells (all vertex level-set values are negative), and  $\alpha_s = 0.5$  for cut sub-cells. We set the maximal subdivision level to be 5 for 2D simulations investigated here. For 3D simulations, this algorithm is computationally costly. We prefer to use the volume-estimation method of Ref. [23] (see Appendix A therein) or a recently derived analytical formulation [27].

### 2.3.1. Conservation correction for a multi-material-cell

For the material  $\chi$  summing Eq. (13) over its material domain  $\Omega^\chi$  yields

$$\sum_{i,j} \alpha_{i,j}^{\chi,n+1} \mathbf{U}_{i,j}^{n+1} = \sum_{i,j} \alpha_{i,j}^{\chi,n} \mathbf{U}_{i,j}^n + \sum_{i,j} \frac{\Delta t}{\Delta x \Delta y} \hat{\mathbf{X}}(\Delta \Omega_{i,j}^\chi) + \text{boundary terms} \quad (14)$$

For two-phase flows, overall conservation can be achieved by summing Eq. (14) for the two fluids because interface-exchange terms in cut cell always have opposite sign for each of the interacting materials, and the sum of volume fractions of the two fluids equals 1. For multi-material flows, although the volume fractions in a two-material-cell satisfy  $\alpha^{\chi_1} + \alpha^{\chi_2} = 1$ , in a multi-material-cell where more than two materials meet the sum of volume fractions may be  $\sum_{r \in \mathbf{X}_s} \alpha^{\chi_r} \neq 1.0$  if we assume that the material boundary segments are piecewise linear inside the cell. For example in Fig. 2(a), the linear material boundary segments of three materials never coincide, resulting in a void region, and thus  $\alpha^a + \alpha^b + \alpha^c < 1.0$ . To correct this total volume fraction deficiency, the piecewise linear assumption no longer can be applied to this cell. A straightforward way is to explicitly reconstruct the sub-cell topology inside this multi-material-cell as shown in Fig. 2(b). Note that all the three material boundary segments are not linear any longer. The new volume fraction for each material is updated by

$$\alpha^a = \alpha^a + \alpha^{a,*}, \quad \alpha^b = \alpha^b + \alpha^{b,*}, \quad \alpha^c = \alpha^c + \alpha^{c,*}. \quad (15)$$

Although this procedure is considered to be accurate as long as the explicit reconstruction method is sufficiently accurate, it is computationally expensive, especially in three dimensions. An alternative efficient way is shown in Fig. 2(c). Instead of explicitly

reconstructing the sub-cell structure, we only modify the volume fraction corresponding to the smallest mass fraction inside this cell:

$$\alpha^{\chi^*} = \alpha^{\chi^*} + \alpha^{\chi^*,*}, \quad \alpha^{\chi^*,*} = 1 - \sum \alpha^\chi, \quad \chi^* = \arg \min_{\chi} (\alpha^\chi \rho_\chi). \quad (16)$$

Thus this method is efficient especially in 3D as no reconstruction is needed. Although it does not resolve the sub-cell structure and is generally less accurate than the first method, the error is limited as the material dominating the cell properties (labelled by the primary indicator) has a volume fraction larger than 0.5 which is not affected by the correction.

### 2.3.2. Material interface interaction model

The interface interaction for each connected material pair  $(\Omega^\xi, \Omega^\eta)$  occurs at the pairwise interface  $\Gamma_{\xi\eta}$  and can be described by a Riemann problem. The solution of this Riemann problem produces the interface condition which is used to calculate the exchange flux  $\hat{\mathbf{X}}$  in Eq. (13) and the interface advection velocity  $\mathbf{v}$  in Eq. (7). Hu et. al [24] have shown that the HLLC Riemann solver [28] is robust, accurate and efficient in handling two-phase flow with very strong interactions and large jumps of material properties. In this paper, we employ this approach to solve multi-material interface interactions.

Consider that the finite-volume cell  $C_{i,j}$  in Fig. 3(a) is occupied by three materials  $a$ ,  $b$  and  $c$ , which are colored by blue, red and green, respectively. [With our method, the multi-material cell  \$C\_{i,j}\$  contains one regional level-set  \$\varphi\_{i,j}^\chi\$  and multiple fluid states. For the cell in Fig. 3\(a\), the flow states of material  \$a\$  are obtained by solving Eq. \(13\), and the states of the other material are extended from the respective material domains by using the extending algorithm \[15, 18\].](#) According to Fig. 3(b), the interface condition at each pairwise interface segment  $\Gamma_{\xi\eta}$  is obtained by solving a corresponding 1D Riemann problem  $R(W_L, W_R)$  along a local normal direction  $\mathbf{n}_{\xi\eta}$  of  $\Gamma_{\xi\eta}$ . The constant left and right states of the Riemann problem,  $(W_L, W_R)$ , are defined as

$$(W_L, W_R) = \begin{cases} (\hat{W}_\xi, \hat{W}_\eta) & \text{if } \alpha^\xi \rho_\xi < \alpha^\eta \rho_\eta \\ (\hat{W}_\eta, \hat{W}_\xi) & \text{otherwise} \end{cases}, \quad \hat{W}_\xi = \begin{cases} W_\xi & \text{if } \xi = \chi_1 \\ W_\xi^g & \text{otherwise} \end{cases}, \quad (17)$$

where the superscript “g” indicates the ghost state at the cell center and  $\chi_1$  is the primary material indicator with  $\alpha^{\chi_1} > 0.5$ . We rewrite the EOS with a general form

$$p = p(\rho, e), \quad (18)$$

and the speed of sound

$$c_s = \left. \frac{\partial p}{\partial \rho} \right|_e + \frac{p}{\rho^2} \left. \frac{\partial p}{\partial e} \right|_\rho = \Psi + \Upsilon \frac{p}{\rho}, \quad (19)$$

where  $\Upsilon$  is the Grüneisen coefficient and  $\Psi$  determines the material properties [24]. Afterwards, the HLLC approximate Riemann solver is invoked to obtain the two intermediate states,  $W_{\xi\eta}^{*,L}$  and  $W_{\xi\eta}^{*,R}$ , see Fig. 3(b), which have the relation

$$u_{\xi\eta}^{*,L} = u_{\xi\eta}^{*,R} = S_M = u^*, \quad p_{\xi\eta}^{*,L} = p_{\xi\eta}^{*,R} = p^*, \quad (20)$$

where  $S_M$  is the speed of the contact wave or the material interface. Toro et al. [28] use the jump conditions and the integral form of the conservation law to obtain the normal contact wave velocity

$$u^* = S_M = \frac{(S_R - u_R)\rho_R u_R + (u_L - S_L)\rho_L u_L + p_L - p_R}{(S_R - u_R)\rho_R + (u_L - S_L)\rho_L} \quad (21)$$

and the intermediate pressure

$$p^* = p_L + \rho_L(S_L - u_L)(S_M - u_L) = p_R + \rho_R(S_R - u_R)(S_M - u_R) \quad (22)$$

which describe the interface condition. The minimum and maximum wave speed  $S_L$  and  $S_R$  are estimated by

$$S_L = \min[u_L - c_{s,L}, \tilde{u} - \tilde{c}_s], \quad S_R = \max[\tilde{u} + \tilde{c}_s, u_R + c_{s,R}]. \quad (23)$$

For two adjacent states described by different EOS, the average speed of sound  $\tilde{c}_s$  is obtained by

$$\tilde{c}_s^2 = \tilde{\Psi} + \tilde{\Upsilon} \left( \widetilde{\frac{p}{\rho}} \right), \quad (24)$$

where the tilde on the right side indicates Roe-averaged values

$$\tilde{\rho} = \sqrt{\rho_L \rho_R}, \quad \tilde{f} = \mu(f) = \frac{\sqrt{\rho_L} f_L + \sqrt{\rho_R} f_R}{\sqrt{\rho_L} + \sqrt{\rho_R}}, \quad f = \Psi, \Upsilon \quad (25)$$



and

$$\widetilde{\left(\frac{p}{\rho}\right)} = \mu \left(\frac{p}{\rho}\right) + \frac{1}{2} \tilde{\rho} \left(\frac{u_R - u_L}{\sqrt{\rho_L} + \sqrt{\rho_R}}\right)^2. \quad (26)$$

We can calculate the interface flux between materials  $\xi$  and  $\eta$  according to the interface condition  $(\mathbf{u}_{\xi\eta}^*, p_{\xi\eta}^*)$  obtained above, where  $\mathbf{u}_{\xi\eta}^* = u_{\xi\eta}^* \mathbf{n}_{\xi\eta}$ . For a two-material-cell, the flux  $\hat{\mathbf{X}}$  in Eq. (13) has the same form as that in Ref. [11]. The multi-material-cell, e.g. the three-material-cell in Fig. 3, has the more complex interface flux

$$\begin{aligned} \hat{\mathbf{X}}(\Delta\Omega_{i,j}^a) &= \hat{\mathbf{X}}(\Delta\Gamma_{ab}) + \hat{\mathbf{X}}(\Delta\Gamma_{ac}) = \hat{\mathbf{X}}(\Delta\Gamma_{\overline{OA}}) + \hat{\mathbf{X}}(\Delta\Gamma_{\overline{OC}}) \\ \hat{\mathbf{X}}(\Delta\Omega_{i,j}^b) &= -\hat{\mathbf{X}}(\Delta\Gamma_{ab}) - \hat{\mathbf{X}}(\Delta\Gamma_{bc}) = -\hat{\mathbf{X}}(\Delta\Gamma_{\overline{OA}}) - \hat{\mathbf{X}}(\Delta\Gamma_{\overline{OB}}) \quad , \\ \hat{\mathbf{X}}(\Delta\Omega_{i,j}^c) &= \hat{\mathbf{X}}(\Delta\Gamma_{bc}) - \hat{\mathbf{X}}(\Delta\Gamma_{ac}) = \hat{\mathbf{X}}(\Delta\Gamma_{\overline{OB}}) - \hat{\mathbf{X}}(\Delta\Gamma_{\overline{OC}}) \end{aligned} \quad (27)$$

where the interface inside the cell,  $\Delta\Gamma_{\overline{OC}}$ , are the line segments shown in Fig. 13(b). The interface condition is used to calculate these fluxes, e.g.

$$\hat{\mathbf{X}}(\Delta\Gamma_{\overline{OA}}) = [0, p_{ab}^* \Delta\Gamma_{\overline{OA}} \mathbf{n}_{ab}^x, p_{ab}^* \Delta\Gamma_{\overline{OA}} \mathbf{n}_{ab}^y, p_{ab}^* \Delta\Gamma_{\overline{OA}} \mathbf{n}_{ab} \cdot \mathbf{u}_{ab}^*]^T. \quad (28)$$

This model represents the full set of interactions. However, it is computationally expensive due to the fact that an explicit reconstruction of the interface-network is necessary to calculate the length and normal direction of  $\Delta\Gamma_{\overline{OA}}$ ,  $\Delta\Gamma_{\overline{OB}}$  and  $\Delta\Gamma_{\overline{OC}}$ . Moreover, it is difficult to extend to 3D since the number of interface segments for each material may become very large. As alternative, we propose a reduced interaction model for a multi-material-cell. The basic idea is that one only considers the interaction between the two materials with largest mass fraction inside a multi-material-cell. Assuming the mass fraction of each material is ordered as  $\alpha^a \rho_a > \alpha^b \rho_b > \alpha^c \rho_c$  in Fig. 13, the reduced model is

$$\begin{aligned} \hat{\mathbf{X}}(\Delta\Omega_{i,j}^a) &= \hat{\mathbf{X}}(\Delta\Gamma_{ab}) \approx \hat{\mathbf{X}}(\Delta\Omega_{\overline{AC}}^a) \\ \hat{\mathbf{X}}(\Delta\Omega_{i,j}^b) &= -\hat{\mathbf{X}}(\Delta\Gamma_{ab}) \approx -\hat{\mathbf{X}}(\Delta\Omega_{\overline{AC}}^a), \end{aligned} \quad (29)$$

where  $\Delta\Omega_{\overline{AC}}^a$  is the material boundary of material  $a$  represented by its local level set. The normal direction  $\mathbf{n}_{\xi\eta}$  in the full interaction model can be approximated by the normal of a particular material boundary. As shown in Fig. 2(a), the three normal directions of material  $a$ ,  $b$  and  $c$  are defined at the cell center and can be calculated by their

corresponding local level-set fields

$$\mathbf{n}_{\chi_r} = \frac{\nabla \phi^r}{|\nabla \phi^r|}, \quad \chi_r = a, b, c. \quad (30)$$

Note that the normal direction points into the respective material. The direction of the local Riemann problem  $R(W_L, W_R)$  is

$$\mathbf{n}_{\xi\eta} = \begin{cases} \mathbf{n}_\xi & \text{if } \alpha^\xi \rho_\xi \geq \alpha^\eta \rho_\eta \\ \mathbf{n}_\eta & \text{otherwise} \end{cases}. \quad (31)$$

Additionally, the interface flux is modified by

$$\hat{\mathbf{X}}(\Delta\Omega_{AC}^a) = [0, p_{ab}^* \Delta\Omega_{AC}^a \mathbf{n}_a^x, p_{ab}^* \Delta\Omega_{AC}^a \mathbf{n}_a^y, p_{ab}^* \Delta\Omega_{AC}^a \mathbf{n}_a \cdot \mathbf{u}_{ab}^*]^T, \quad (32)$$

where  $\mathbf{n}_a$  replaces  $\mathbf{n}_{ac}$  as  $\alpha^a \rho_a > \alpha^c \rho_c$ . The averaged flow variable of the two subvolumes separated by  $\Delta\Omega_{OA}^a$  are  $W_a$  and  $W_b$ , respectively, indicating that the flow state of material  $c$  is approximated by the data of material  $b$ . by this procedure we reduce the multiple interactions to a single interaction, irrespectively of the number of materials inside a cell. Moreover an explicit interface reconstruction no longer is needed to calculate the normal directions. Thus the reduced model significantly improves computational efficiency, especially in 3D.

The rationale of the reduced-model formulation is based on the assumption that the material with largest mass fraction  $\alpha_a \rho_a$  in a multi-material cell usually dominates the inerial dynamics. Under this assumption it suffices to determine is the interaction between this material  $a$  with the mixture of  $b$  and  $c$ , without resolving the subcell details of the multi-material interactions. The flow state  $\mathbf{U}_m$  of the mixture (denoted by “m”) can be determined following e.g. [29],

$$\rho_m = \sum_{r=b,c} \alpha_r \rho_r, \quad (\rho \mathbf{u})_m = \sum_{r=b,c} \alpha_r \rho_r \mathbf{u}_r, \quad (\rho E)_m = \sum_{r=b,c} \alpha_r \rho_r (e_r + \frac{1}{2} |\mathbf{u}_r|^2), \quad (33)$$

where the volume fractions have been normalized by the total volume of the mixture  $\sum_{r=b,c} \alpha_r$ . If the mass fraction of  $c$  is sufficiently small,

$$\alpha_c \rho_c \ll \alpha_b \rho_b, \quad (34)$$

and the density of the materials constituting the mixture satisfies

$$\rho_c \simeq \rho_b, \quad (35)$$

the state of the mixture can be approximated by

$$\rho_m \simeq \rho_b, \quad (\rho \mathbf{u})_m \simeq \rho_b \mathbf{u}_b, \quad (\rho E)_m \simeq \rho_b (e_b + \frac{1}{2} |\mathbf{u}_b|^2). \quad (36)$$

which essentially implies that the interaction between material  $a$  and the mixture  $m$  can be replaced by the interaction of the reduced model (29). Note that for highly compressible flow, the assumptions (34) and (35) may be not valid. Nevertheless even for complex test cases shown in Sec. 3, Eq. (29) produces good results with high computational efficiency.

Global conservation is also achieved as can be seen from summing over all materials

$$\sum_{\chi \in \mathbf{X}} \sum_{i,j} \alpha_{i,j}^{\chi,n+1} \mathbf{U}_{i,j}^{n+1} = \sum_{\chi \in \mathbf{X}} \sum_{i,j} \alpha_{i,j}^{\chi,n} \mathbf{U}_{i,j}^n + \text{boundary terms}. \quad (37)$$

The interface fluxes for the two interacting materials have opposite sign in all multi-material-cells, i.e.  $\hat{\mathbf{X}}(\Delta \Omega_{i,j}^\xi) + \hat{\mathbf{X}}(\Delta \Omega_{i,j}^\eta) = 0$ . Although the reduced model simplifies the interface interaction and produces good results for the test cases in Sec. 3, numerical artifact may be generated for more complex problems where different materials may not be described by same type of governing equation, e.g. fluid-solid interaction problems [30].

Note that the small volume fraction of a particular material may lead to numerical instability if the time step of an explicit time integration scheme is calculated according to the full cell CFL condition. In order to maintain numerical stability without reducing the time step, we apply the mixing procedure [18] after each Runge-Kutta sub-step. For each material, the conservative quantities of a small volume fraction cell are mixed with those of the larger neighboring cells in a conservative way. The exchanges of the conservative quantities  $\mathbf{M}$  are calculated according to the averaged values, see Ref. [18]. The conservative quantities for each material in the near interface cells are updated by

$$\alpha_{i,j}^{\chi,n+1} \mathbf{U}_{i,j}^{n+1} = (\alpha_{i,j}^{\chi,n+1} \mathbf{U}_{i,j}^{n+1})^* + \sum \mathbf{M}^x + \sum \mathbf{M}^y, \quad (38)$$

where the second and third terms on the right hand side represent the sum of all mixing exchanges of cell  $C_{i,j}$  in the  $x$  and  $y$  directions, respectively.

The coupling between the interface capturing method in Sec. 2.2 and the fluid evolution described by Eq. (13) is as follows. Given conservative flow states  $\alpha^n \mathbf{U}^n$  and the

regional level-set function  $\varphi^{\chi,n}$  at the time step  $n$ , the procedure to predict both the interface  $\varphi^{\chi,n+1}$  and the conservative flow states  $\alpha^{n+1}\mathbf{U}^{n+1}$  at the next time step  $n+1$  involves the following sequences:

- Update the volume fraction  $\alpha^n$ , aperture  $A$ , and normal direction  $\mathbf{n}$  using the regional level-set function.
- Update the flow states  $\mathbf{U}^n$  by  $\mathbf{U}^n = \alpha^n \mathbf{U}^n / \alpha^n$ .
- For each material  $\chi$ , extend the fluid states defined on  $\Omega^\chi$  to the ghost fluid domain  $\Omega \setminus \Omega^\chi$ .
- Solve the material interaction to obtain the exchange flux  $\hat{\mathbf{X}}$  and the interface velocity  $\mathbf{u}^*$  by the reduced model (29).
- Evolve the conservative flow states by Eq. (13) to obtain  $\alpha^{n+1}\mathbf{U}^{n+1}$ .
- Solve the interface advection equation (7) to obtain the new regional level-set function  $\varphi^{\chi,n+1}$ .
- Invoke the mixing procedure (38) for small cut cells.

### 2.3.3. Interface scale separation model

In this section, we discuss a numerical procedure for consistent removal of non-resolved interface segments during multi-material simulations. For a given spatial resolution non-resolved interfacial scales, such as thin filaments and small droplets, need to be removed in order to avoid proliferation of artifacts. For this purpose, the separation of resolvable and non-resolvable interface scales is necessary. The scale separation operation for two-material-cells is performed with the model in Refs. [22, 23] without need for modifications. In multi-material-cells non-resolved interface structures may occur across different material domains, so that the scale separation model must be adaptated to multi-material interfaces. After the removal of non-resolved structures the new interface needs to be constructed between these materials in such a way that these different materials stay separated, however with a different connection relation.

The basic idea of the multi-material-interface scale separation model resembles that of the two-material model [22, 23]: each material domain is simply connected as long as the

interface is resolved; non-resolved interface segments, however, show up as not simply connected sub-domains when the level-set field is slightly shifted. This observation is used to find "oddball cells" where non-resolved interface segments exist. We define the  $\epsilon^\pm$ -material-interface as

$$\Gamma_{\epsilon^\pm}^\chi = \{\mathbf{x} \in \Omega^\chi | \phi^\chi(\mathbf{x}) \pm \epsilon = 0, \chi \in \mathbf{X}\} \quad (39)$$

where  $\epsilon$  is a small positive parameter [22] and can be set to  $0.75h$  for 2D and  $0.9h$  for 3D in order to remove interface segment whose scales are smaller than grid scale  $h$  [22]. The set of cut cells  $S_0$  which contains the segments of the interface network is defined as

$$S_0 = \{C_{i,j} | \partial C_{i,j} \cap \Gamma \neq \emptyset\}. \quad (40)$$

For each material  $\chi$  we define  $S_\pm^\chi$  as the sets of cut cells containing the segments of  $\partial\Omega_{\epsilon^\pm}^\chi$

$$S_\pm^\chi = \{C_{i,j} | \partial C_{i,j} \cap \partial\Omega_{\epsilon^\pm}^\chi \neq \emptyset\}. \quad (41)$$

The scale separation operation consists of three main steps. First, we identify the oddball cells where non-resolved interface segments reside. The selection criterion of oddball cells is similar as that of Ref. [23], which requires that to each oddball no neighbour exists that belongs to  $S_-^{\chi_1}$

$$S_* = \{C_{i,j} | (C_{i,j} \in S_0) \wedge (\forall i_0, j_0 \in \{-1, 0, 1\}, C_{i+i_0, j+j_0} \notin S_-^{\chi_1})\}, \quad (42)$$

where  $\chi_1 = \chi_{i,j}$  is the primary indicator of  $C_{i,j}$ . Second, the local non-resolved topology of the oddball cell in  $S_*$  is altered to a new resolved topology by replacing its indicator with the indicator corresponding to the second largest volume fraction

$$\chi_1^* = \arg \max_{\chi_r \neq \chi_1} \alpha_{\chi_r} \quad (43)$$

as changing from  $\chi_1$  to  $\chi_1^*$  requires the least stimulus of level-set values for this cell and thus  $\chi_1^*$  has the largest possibility to occupy this cell after scale separation. Note that this procedure automatically generates a new interface. Third, the unsigned distance function of cell containing non-resolved interface segment is assigned with new data that fit the interface network of the new resolved topology. This is accomplished by the same

operation as in Ref. [23]. Because the considered cell  $C_{i,j}$  in  $S_*$  belongs to  $\Omega^{\chi_1^*}$  after scale separation, we calculate the distance from its center to  $\partial\Omega_{\epsilon^+}^{\chi_1^*}$

$$d = \sqrt{[i - i_0\Delta x + (\varphi_{i_0,j_0} + \epsilon)n_x]^2 + [j - j_0\Delta y + (\varphi_{i_0,j_0} + \epsilon)n_y]^2}, \quad (44)$$

where  $(i_0, j_0)$  is the index pair of the cell in  $S_+^{\chi_1^*}$  within a search stencil  $i - 3 \leq i_0 \leq i + 3, j - 3 \leq j_0 \leq j + 3$ .  $\{n_x, n_y\}$  is the unit normal vector at the center of  $C_{i_0,j_0}$ . Subsequently, we update the regional level-set with

$$\phi_{i,j}^* = (\varphi_{i,j}^*, \chi_1^*), \quad \varphi_{i,j}^* = |d_{min} - \epsilon|. \quad (45)$$

Fig. 4 shows two illustrative test cases (a thin filament and a small droplet) where non-resolved interface scales exist. The computational domain is a unit square with the grid size  $\Delta x = \Delta y = 0.1$ . The thickness of the thin filament is  $1.2\Delta x$ , and the radius of the small droplet is  $1.5\Delta x$ . In Fig. 4(a), two interfaces that separates three materials merge to one after using the scale separation model, indicating that the material in the filament is entirely removed. The small droplet in Fig. 4(b) becomes an isolated bubble and the filament connecting the droplet and the main body collapses to a single interface while the other interface segments remain invariant. Two additional triple points are generated as expected. The level-set contours remain regular after scale separation and the contours inside the bubble do not change by the scale-separation operation, as shown in Figs. 4(c) and 4(d).

#### 2.4. Space-time adaptivity

To achieve high computational efficiency and low memory storage, the space-time adaptivity strategy developed in Ref. [25] is incorporated into our compressible multi-material method with minor changes. In detail, the multi-resolution method [31] is used for mesh refinement due to its high rate of data compression. The projection and prediction operators [32] are defined based on the cell-averaged multi-resolution representation. For simplicity, the 1D operators with 5th-order interpolation are

$$P_{\ell+1 \rightarrow \ell} : \quad \bar{u}_{\ell,i} = \frac{1}{2}(\bar{u}_{\ell+1,2i} + \bar{u}_{\ell+1,2i+1}), \quad (46)$$

and

$$\begin{aligned}
P_{\ell \rightarrow \ell+1} : \quad \hat{u}_{\ell+1,2i} &= \bar{u}_{\ell,i} + \sum_{m=1}^2 \gamma_m (\bar{u}_{\ell,i+m} + \bar{u}_{\ell,i-m}), \\
\hat{u}_{\ell+1,2i+1} &= \bar{u}_{\ell,i} - \sum_{m=1}^2 \gamma_m (\bar{u}_{\ell,i+m} + \bar{u}_{\ell,i-m}),
\end{aligned} \tag{47}$$

where  $\ell$  is the index of levels, and  $\gamma_m$  is the interpolation coefficient. Mesh refinement and coarsening are accomplished by comparing the prediction error  $\bar{d}_{\ell,i} = \bar{u}_{\ell,i} - \hat{u}_{\ell,i}$  with a level-dependent threshold [25]. A multi-step Runge-Kutta local time stepping scheme [33] is employed to achieve time adaptivity and thus obtain additional speed-up. To maintain strict conservation a conservative flux correction [33] is adopted between cells with different levels.

The pyramid data structure and storage-and-operation-splitting approach proposed in Ref. [25] are used here. The block containing cells which reside in the narrow band of the interface network is refined to the finest level  $\ell_{max}$  and denoted as “multi-material block”, otherwise as “single-material block”. In such way operations related to the interface, including interface interaction, mixing procedure, scale separation and level-set advection, are only conducted at the finest level. The block position identifier [25] is used to distinguish the block location. The identifier at the finest level is 1 whenever the block has cells which occur in the narrow band of any cut cell, otherwise it is 0. A cell  $C_{i,j}$  contains the interface network if it is intersected by the zero contour of local level-set field

$$\exists r \in X_s, C_{i,j} \cap \{\mathbf{x} | \phi^r(\mathbf{x}) = 0\} \neq \emptyset, \tag{48}$$

or the indicator field in  $V_s$  differs from  $\chi_{i,j}$ ,

$$\exists C_{k,l} \in V_s, \chi_{k,l} \neq \chi_{i,j}. \tag{49}$$

The position identifier of blocks at other levels are obtained according to Ref. [25]. The final multi-resolution representation of a multi-material problem is generated by locations of interface and shock waves, see e.g. Fig. 5.

Note that a “single-material block” may also exist at the finest level if a shock wave resides in this block. For a “multi-material block”, we allocate memory for one single regional level-set field and  $\mathcal{N}_b$  flow state fields, where  $\mathcal{N}_b$  is determined by searching all

unique indicator inside the inner and buffer zone of this block and satisfies the relation  $\mathcal{N}_b \ll \mathcal{N}$  when  $\mathcal{N}$  is large. For a “single-material block”, the volume fraction and apertures become unity, and the interface exchange terms vanish. Thus the governing equation Eq. (13) degenerates to a standard finite volume scheme on a Cartesian grid.

### 3. Numerical validation

In this section, we assess the accuracy and robustness of the present method by a number of test cases. The materials are assumed to be inviscid compressible fluids whose dynamics are governed by Eq. (1), with different EOSs for different materials. As the interaction between each material pair can be cast as Eq. (29), our reduced model works well for the test cases below. However, a model extension may be required for other types of materials. Although a recently developed interface extraction algorithm [34] efficiently determines the sub-cell interface geometrical information (normal direction and volume fraction), the development of an efficient full interaction model is not straightforward. Applications of the present numerical model are limited to fluid-like materials.

First, the 1D multi-material shock tube and ICF implosion are considered. Then more complex 2D cases, including 2D ICF implosion, compressible triple point and shock wave interactions in multiple materials serve to demonstrate the robustness of the interface interaction model and multi-material scale separation method in high-resolution simulations. For all test cases, discretization of the flow and interface evolution equation is performed by a 5th-order WENO [35] and a 2nd-order strongly stable Runge-Kutta scheme [36], with a CFL number of 0.6.

#### 3.1. Shock-tube problem (I)

The three-material shock-tube problem of two helium gases and one air gas modeled by an ideal-gas EOS is an extension of the two-material shock-tube problem in Refs. [18, 15]. Reflective boundary conditions are applied at  $x = 0$  and  $x = 1$ . The initial condition is listed in Table. 1. The grid spacing is  $\Delta x = 5.0 \times 10^{-3}$  which we compare with a high-resolution result with  $\Delta x = 2.5 \times 10^{-4}$ . At  $t = 0$ , two Riemann problems occur at  $x = 0.4$  and  $x = 0.6$  and generate symmetric wave types. Two shock waves move towards the left and right boundaries while two rarefaction waves approach to



Table 1: Initial conditions for 1D test cases I and III.

	Case I*			Case III		
Location	$0 \leq x < 0.4$	$0.4 \leq x < 0.6$	$0.6 \leq x \leq 1.0$	$0 \leq r < 1.0$	$1.0 \leq r < 1.2$	$1.2 \leq r \leq 1.5$
$\chi$	1	2	3	1	2	3
$\rho$	0.125	1.0	0.125	0.05	1.0	0.1
$p$	0.1	1.0	0.1	0.1	0.1	13.0
$\gamma$	1.667	1.4	1.667	1.667	1.667	1.667

Note: the velocity  $u$  is zero everywhere.

\* For the helium-air-R22 shock tube problem, just change  $\gamma$  to 1.249 in  $0.6 \leq x \leq 1.0$ .

each other. Finally, at  $t = 0.1$  these two rarefaction waves impact and interact with each other, as shown in Fig. 6. Good agreement with the reference solution is observed and the distributions of flow variables exhibits symmetric profiles. When we modify the ratio of specific heats in  $0.5 \leq x \leq 1.0$  to R22, i.e.  $\gamma = 1.249$ . The problem becomes asymmetric, as can be seen in Fig. 6. The results demonstrate the conservation of mass for each individual material.

### 3.2. 1D Explosive driving and high-speed impact problem (II)

Now we consider three-material explosive driving and high-speed impact problems which contain more complex EOS. Following Refs. [37, 29, 24], we model the explosive by the JWL EOS

$$p = A_0 \exp\left(\frac{-R_1 \rho_0}{\rho}\right) \left(1 - \frac{\rho}{R_1 \rho_0}\right) + B_0 \exp\left(\frac{-R_2 \rho_0}{\rho}\right) \left(1 - \frac{\rho}{R_2 \rho_0}\right) + \Gamma_0 \rho (e + e_0), \quad (50)$$

and the impacting materials by the MG EOS,

$$p = p_r + \Gamma(\rho) \rho (e - \frac{1}{2} p_r \frac{\rho - \rho_0}{\rho \rho_0}), \quad (51)$$

where

$$p_r = \rho_0 c_0^2 \frac{1 - \rho_0/\rho}{(1 - S(1 - \rho_0/\rho))^2} \quad \text{and} \quad \Gamma(\rho) = \frac{\rho_0}{\rho} \Gamma_0. \quad (52)$$

The constants in Eqs. (50) and (52),  $\Gamma_0$ ,  $\rho_0$ ,  $A_0$ ,  $B_0$ ,  $R_1$ ,  $R_2$ ,  $e_0$ ,  $c_0$ ,  $S$ , are listed in Table 2 for different materials. The mesh resolution and boundary conditions are the same with those of the above shock-tube case. First we test a symmetric configuration

Table 2: Initial conditions and EOS parameters for 1D copper-TNT-copper and aluminum-TNT-copper impact problems.

	Case II*		
Location	$0 \leq x < 0.3$ (copper plate)	$0.3 \leq x < 0.7$ (detonation products)	$0.7 \leq x \leq 1.0$ (copper plate)
$\chi$	1	2	3
$\rho$	8.924	2.48537	8.924
$p$	0	37	0
$\Gamma_0$	1.96	0.25	1.96
$\rho_0$	8.924	1.84	8.924
$A_0$	/	854.5	/
$B_0$	/	20.5	/
$R_1$	/	4.6	/
$R_2$	/	1.35	/
$e_0$	/	8.15	/
$c_0$	3.91	/	3.91
$S$	1.51	/	1.51

Note: the velocity  $u$  is zero everywhere.

\* For the aluminum-TNT-copper impact problem, just change  $\rho$  to 2.785 in  $0 \leq x < 0.3$ . Its EOS parameters are modified by  $\Gamma_0 = 3$ ,  $\rho_0 = 2.785$ ,  $c_0 = 5.238$ , and  $S = 1.338$ .

where the domain is decomposed into three parts: (i) a copper plate ( $0 \leq x < 0.3$ ), (ii) a product gas of the explosive TNT ( $0.3 < x \leq 0.7$ ), and (iii) another copper plate ( $0.7 < x \leq 1$ ). The initial condition is shown in Table 2, and the final time is  $t = 0.05$ . Then we replace the material of the first part ( $0 \leq x < 0.3$ ) by an aluminum plate. As shown in Fig. 7, our coarse-resolution ( $\Delta x = 5.0 \times 10^{-3}$ ) numerical results agree well with high-resolution results ( $\Delta x = 2.5 \times 10^{-4}$ ).

### 3.3. 1D Cylindrical ICF implosion (III)

The setup of the ICF implosion simulations in a cylindrical geometry is taken from Ref. [38]. The computational domain is  $[0, 1]$  and 1D axisymmetrical grids with different resolutions are used. There are three materials in the domain. A light fluid is located in the core region of the target and is surrounded by a shell of dense fluid. Outside the shell is an ambient material which is not solved during the simulation. Thus we treat the interface between the shell and the ambient material as a free surface boundary. To drive the implosion the pressures  $p(t)$  imposed on that boundary are initially constant

and then decrease linearly as

$$p(t) = 13 - \frac{12.5(t - 0.04)}{0.125 - 0.04}, \quad (53)$$

according to Ref. [38].

The evolution of the locations of inner and outer interfaces of the shell are shown in Fig. 8. Fig. 8(a) shows that our results converge to the Lagrangian result [38] with the cell number increasing from 160 to 1280. At the initial stage the outer interface moves inward under a constant pressure, leading to a shrinking of the shell until  $t = 0.047$ . Both the interfaces move towards the core. As the contraction speed of the inner interface is larger than that of the outer one, the thickness of the shell increases. The deceleration of the light fluid is observed from  $t = 0.17$  to  $t = 0.24$  when the radius of inner interface reaches its minimum value (referred to as “stagnation time” [38]). Afterwards the light fluid exhibits a expansion.

In order to demonstrate the versatility of the method, we conduct multiple simulations with varying parameters  $r_2$  and  $\gamma_2$ , which are the radius of the outer interface and the ratio of specific heats of the heavy fluid, respectively. Such a parameter study represents a typical design issue for an ICF capsule, as the thickness of the shell and the EOS used in the previous simulations [38] are not realistic. As shown in Fig. 9(a), the thickness of the shell during the simulation, the stagnation time and the compression rate reduce with the initial thickness  $\Delta r = r_2 - r_1$  decreasing from 0.30 to 0.05. When the ratio  $\gamma_2/\gamma_1$  varies from 1.0 to 10.0, the profiles for the inner and outer interfaces are shifted downwards and upwards, respectively, as shown in Fig. 9(b). Thus the achieved minimum radius of inner interface decreases as  $\gamma_2/\gamma_1$  increase, indicating that stiffer shell materials generate higher compression rates.

### 3.4. Compressible triple point problem (IV)

In this section we consider a compressible triple point problem which contains three perfect gases and is often used to validate the accuracy and robustness of Lagrangian or ALE methods for multi-material compressible flow simulations [38, 39]. The computational domain is a rectangle  $[0, 7] \times [0, 3]$  and is partitioned into three sub-domains: (i)  $[0, 1] \times [0, 3]$  which is filled with a high pressure high density fluid  $(\rho, p, \gamma, \chi) = (1, 1, 1.5, 1)$ , (ii)  $[1, 1] \times [0, 1.5]$  which is occupied by a low pressure high density fluid  $(\rho, p, \gamma, \chi) =$

(1, 0.1, 1.4, 2), and (iii)  $[1, 7] \times [1.5, 3]$  which has a low pressure low density flow state  $(\rho, p, \gamma, \chi) = (0.125, 0.1, 1.5, 3)$ . Accordingly, a triple point exists initially at (1, 1.5). Reflective boundary conditions are employed, and the final time of the simulation is 5.0. The coarsest level has  $7 \times 3$  blocks and are refined to the finest level by the mesh refinement criterion in Sec. 2.4.

First, we show numerical results of a high-resolution simulation conducted with  $\ell_{max} = 5$  and an effective resolution of  $3584 \times 1536$  at the finest level. Upon comparing Fig. 10 with previous results in the literature [38, 40], it can be seen that the internal energy contours at  $t = 0.2, 1.0, 3.0, 3.5, 4.0$  and 5.0 are in good agreement. The development of the shock system is illustrated in Fig. 11. The initial Riemann problems at the discontinuities  $\Gamma_{13}$  and  $\Gamma_{12}$  generate a contact discontinuity ( $C1$  or  $C2$ ), a leftward rarefaction wave ( $R1$  or  $R2$ ) and a rightward shock wave ( $S1$  or  $S2$ ), see Fig. 11(a). The shock  $S1$  moves faster than  $S2$  as the acoustic impedance has a relation  $\rho_2 c_{s,2} > \rho_3 c_{s,3}$ . As a consequence, a distinct roll-up region appears around the triple point, as shown in Fig. 11(b). Near the triple point the shock reflection pattern is more complex as different waves interact with each other. Meanwhile, the development of disturbance can be observed in Fig. 11(c) due to the strong shear along all contact discontinuities  $C1$ ,  $C2$  and  $C3$ , which is not observed in numerical results of previous papers [38, 40] and is indicative of less numerical dissipation. Fig. 11(d) shows the shock wave system just after  $S1$  impacts the right boundary and is reflected. At this time instant, the interface inside the roll-up is strongly perturbed, leading to the shedding of small droplets. Afterwards,  $S1$  moves upstream and is partially refracted to generate a transmitted shock  $TS1$ , as shown in Fig. 11(e). After  $S1$  has reached the contact discontinuity  $C1$ , it becomes a transmitted shock  $TS2$  inside the material 1 and a reflected shock  $RS1$  is produced to maintain the mechanical equilibrium at the interface  $\Gamma_{13}$ , see Fig. 11(f). Due to the Kelvin-Helmholtz instabilities along the contact discontinuities, vortical structures are produced, as shown in Fig. 12. The volume fraction contours, computed by the recursive subdivision algorithm [25], are consistent with the density gradient contours and interface locations for all materials, as shown in Fig. 13.

In Fig. 14 we compare our numerical method with the ALE method [41] and curvilinear finite element method [42]. Generally all methods generate similar large roll-up

structure and shock reflection patterns at  $t = 0.5$ . For our method, the filament of the roll-up breaks up into more droplets when the grid resolution is refined, as shown in Figs. 14(a) and (c). This is also observed with the ALE simulations of Ref. [41], see Figs. 14(b) and (d). This phenomenon can be attributed to smaller numerical dissipations for finer grid resolution, as explained by Ref. [41]. Also in our simulations physical interface instabilities are significantly enhanced with decreasing grid size. It is reasonable to expect small-scale Kelvin-Helmholtz instabilities along the contact discontinuities (e.g. C3) for the inviscid flow motion. For high resolution simulations, the roll-up structures and small features inside the primary vortex core are consistent with the results of a curvilinear finite-element method [42], see Figs. 14(e) and (f). Furthermore, a grid resolution study in Fig. 15(a) shows that high-resolutions allow finer resolved scales to develop, as can be expected for a formally inviscid computation with low numerical dissipation. As shown in Fig. 15(b), the interface locations at the upper and lower boundaries also exhibit grid convergence. At  $t = 4.0$ , the shock waves and contact discontinuities corresponding to Fig. 11(e) are represented by the pressure and density profiles along the  $x$  direction at  $y = 0.5$  and  $y = 2.5$ , see Figs. 15(c) and (d). The pressure and density jumps become sharper with increasing resolution from  $\ell_{max} = 0$  to  $\ell_{max} = 5$  and do not develop any overshoots.

### 3.5. 2D cylindrical ICF implosion with perturbed interface ( $V$ )

Increasing the complexity of the configuration considered in Sec. 3.3, we investigate a 2D cylindrical ICF implosion with initial perturbations. This configuration demonstrates that the method can handle interface and small-scale flow instabilities from linear to highly nonlinear stages. The interface between light and heavy fluid has a single-mode perturbation [38, 43] with

$$r'_0 = r_0[1 + A \cos(m\theta)], \quad (54)$$

where  $r_0$  and  $r'_0$  are the initial unperturbed and perturbed radii of the light fluid, and  $\theta$  is the polar coordinate. The mode number  $m$  is 5 and 47 for low-mode and high-mode perturbations, respectively. The amplitude  $A$  of the initial perturbation is 2% of the wavelength of low-mode perturbation. A free surface boundary condition is prescribed at the outer interface. There is one block at the coarsest level and the maximum refinement

level is  $\ell_{max} = 8$ . With each block containing  $16 \times 16$  inner cells, the effective grid resolution at the finest level is  $4096^2$ . Other parameters follow from the 2D extension of the 1D case in Section 3.3.

Figs. 16 and 17 show four snapshots of the density gradient before and after the stagnation time, respectively. At the early stage,  $t = 0.12$  in Fig. 16, the shock wave passes the inner perturbed interface, and a slight distortion of the shell and light gas bubble is observed due to Richtmyer-Meshkov instability. The length scale in Fig. 16 decreases slowly. After maximum compression, Rayleigh-Taylor instability develops as the high pressure inside the light fluid bubble accelerates the heavy shell. The low-mode instability has grown substantially from the stagnation time, which is confirmed by the rapid increase of the length scale in Fig. 17. Secondary instabilities near the inner interface can be seen, as shown in the snapshot  $t = 0.28$ . At time  $t = 0.40$ , the length scale shown in Fig. 17 indicates that the entire structure has significantly expanded and exhibits small-scale mixing [43]. For the high-mode case, the selected two snapshots in Fig. 18,  $t = 0.22$ ,  $t = 0.27$ , are just before and after the maximum compression time. The outer boundary is composed of 47 fingers and show good symmetry preservation. The mixing zone containing most small scales at  $t = 0.28$  is larger than that at  $t = 0.27$ , see the vorticity contours in Fig. 18. A wide range of resolved small interface scales are generated, indicating our method is very robust due to the multi-material scale separation model.

### 3.6. Shock wave interaction with a multi-material bubble (VI)

This problem represents a complex shock-accelerated inhomogeneous flow [44], and is a combination of a 2D air-helium [45, 18, 46, 25] and an air-R22 [25, 47, 48] shock bubble interaction. A Mach 6.0 shock wave in air interacts with a cylindrical helium bubble with a R22 shell. The computational domain and initial conditions are shown in Fig. 19(a) and Table. 3, respectively. Symmetry boundary conditions are employed at the upper and lower boundaries, while inflow and outflow conditions are prescribed at the left and right boundaries. Simulations are performed with  $4 \times 1$  blocks at the coarsest level and  $\ell_{max} = 7$ , leading to an effective resolution of  $8192 \times 2048$  at the finest level.

In Fig. 20, the density gradient fields and materials distributions at 6 time instants illustrate the development of the shock system and the bubble deformation inside a

medium with inhomogeneous flow states. At  $t = 5.0 \times 10^{-3}$ , the incident shock wave is refracted after crossing the upstream front of the R22 shell. As a result of the acoustic impedance mismatch  $\rho_3 c_{s,3} > \rho_1 c_{s,1}$  at the air-helium interface, the transmitted shock wave has a concave curvature while the shock in the ambient air keeps planar. This convergent shock refraction pattern agrees with the numerical results in Refs. [25, 48]. A reflected shock is generated at the upstream front and then propagates upstream inside the air [49, 44]. When the concave transmitted shock wave impacts on the R22-helium interface, the reflected rarefaction occurs and moves upstream inside the R22 shell. The acoustic impedance mismatch  $\rho_2 c_{s,2} > \rho_3 c_{s,3}$  at the air-helium interface produces a convex transmitted shock inside the helium bubble. This shock propagates downstream and subsequently impacts on the downstream surface of helium bubble. At  $t = 1.0 \times 10^{-2}$ , it moves across the interface entirely and becomes a re-transmitted shock in the R22 material, as shown in Fig. 20(b). Correspondingly, a Mach stem, triple point, slip line and re-transmitted reflected shock (moves to the upstream of the helium bubble in Fig. 20(b)) are produced in R22 material during this process [49]. Along the vertical direction one can observe a “fast-slow-fast-slow-fast” type of shock speed according to definition of Zabusky and Zeng [50]. The deformed helium bubble has a similar shape with previous numerical results [18, 46, 25], although its incident shock is not planar. The materials helium and R22 are accelerated with significantly different shock speed. The global shape is extremely distorted, corresponding to “fast-slow-fast-slow-fast” shock wave, see Figs. 20(c) and 20(d). Several upstream-directed reflected shock waves with different shock strength occur at different locations in either R22 shell or helium bubble. These shocks interact with each other and finally with the reflected shock in Fig. 20(a), see Figs. 20(e) and 20(f). From  $t = 1.0 \times 10^{-2}$  to  $t = 3.0 \times 10^{-2}$ , R22 and helium are mixed with the ambient air. The generation of many isolated R22 and helium droplets are captured by our simulation, as shown in Figs. 20(e) and 20(f) and in Fig. 21. The multi-resolution representation shown in Fig. 20(b) demonstrates that all blocks near the interfaces and the shock structures are refined to the finest level,  $\ell_{max} = 7$ .

### 3.7. Shock wave interaction with an Helium bubble and a water column (VII)

In this case, we consider a combination of shock-helium interaction [45, 18, 46, 25] and shock-water interaction [25, 48, 51], where a helium bubble is initially accelerated

Table 3: Initial conditions for 2D test cases.

Location*	Case VI				Case VII			
	Post-shocked air	Pre-shocked air	Helium bubble	R22 shell	Post-shocked air	Pre-shocked air	Helium bubble	Water column
$\chi$	1	1	2	3	1	1	2	3
$\rho$	1.0	5.268	0.138	3.154	1.0	5.268	0.138	1000.0
$p$	1.0	41.83	1.0	1.0	1.0	41.83	1.0	1.0
$u$	5.752	0.0	0.0	0.0	5.752	0.0	0.0	0.0
$\gamma$ **	1.4	1.4	1.667	1.249	1.4	1.4	1.667	7.15

\* See Fig. 19(a) for details.

\*\* Tait's EOS is used for water column and idea gas EOS is for other gaseous materials.

by a Mach 6.0 planar shock and then impacts on a water column. The computational domain and initial conditions are detailed in Fig. 19(b) and Table. 3 while the boundary conditions are the same as in Sec. 3.6. We refine  $4 \times 1$  blocks at the coarsest level to  $\ell_{max} = 6$  to obtain an effective grid resolution of  $4096 \times 1024$  at the finest level.

We plot 4 density gradient fields in Fig. 22 at  $t = 1.0 \times 10^{-2}$ ,  $1.2 \times 10^{-2}$ ,  $1.5 \times 10^{-2}$  and  $1.8 \times 10^{-2}$ , with helium colored by blue to track its evolution after impact on the water column. Note that the bubble deformation, the transmitted and reflected shocks, and the reflected rarefaction wave at  $t = 1.0 \times 10^{-2}$  are in good agreement with those in Ref. [25], see Fig. 22(a). Triple point, Mach stem and slip line are observed at this time instant. The deformed helium bubble moves downstream and impacts on the water column at  $t = 1.2 \times 10^{-2}$ . A transmitted shock and reflected shock are generated at the helium-water interface. As the speed of sound in helium is comparable with that in water, the transmitted shock in water and re-transmitted shock in the ambient air together form a bow shock wave. Due to the high stiffness of the water column, the helium keeps closely touched to the water column, as shown in Fig. 22(b). From  $t = 1.5 \times 10^{-2}$  to  $t = 1.8 \times 10^{-2}$ , near two roll-up regions of helium propagate across the water column, while little helium material resides along the upstream surface of water column. Small droplets are generated due to the displacement effect of the water column. Complex shock refraction pattern develop, indicating the increased complexity as compared to configuration considered before [49, 44].



#### 4. Conclusion

The proposed conservative multi-material interface-interaction method comprises a multi-region level-set method, a conservative finite volume method, an interface interaction model and an interface scale separation model to overcome typical problems in the numerical simulations of compressible multi-material flows. The advection of interface networks is handled by the multi-region level-set method. Conservation is strictly satisfied by solving the discretized governing equation with multi-material-cell treatments and by using a conservation correction in each multi-material-cell. The sharp interface property is maintained by an efficient reduced interface interaction model to obtain the interface condition which serves to calculate the velocity of the interface network and the exchange flux across different materials, instead of solving the full Riemann problem inside a multi-material-cell. In addition, computational robustness is enhanced by removing non-resolved interface scales with a multi-material interface scale separation model. A range of test cases validates that the proposed method has the intended properties and demonstrates that the method is highly robust, flexible and efficient for simulations of compressible multi-material flows. Although we only consider 1D and 2D test cases in this paper and the flows are restricted to be inviscid, we emphasize that this method is straightforward to implement in 3D and with no difficulties can be extended to viscous compressible flows with source terms such as surface tension and gravity, by modifying the exchange fluxes in the multi-material-cells.

#### Acknowledgment

This work is supported by China Scholarship Council under No. 201306290030. XYH acknowledges funding from national Natural Science Foundation of China (No. 11628206). NAA acknowledges funding from the European Research Council (ERC) under the Horizon 2020 grant agreement No. 667483. We acknowledge Dr. Tzanio Kolev for useful discussion about the triple-point-shock interaction problem.

#### References

- [1] V. A. Thomas, R. J. Kares, Drive asymmetry and the origin of turbulence in an ICF implosion, *Physical Review Letters* 109 (7) (2012) 075004.

- [2] E. J. Lentz, S. W. Bruenn, W. R. Hix, A. Mezzacappa, O. B. Messer, E. Endeve, J. M. Blondin, J. A. Harris, P. Marronetti, K. N. Yakunin, Three-dimensional core-collapse supernova simulated using a  $15\text{ m}_{\odot}$  progenitor, *The Astrophysical Journal Letters* 807 (2) (2015) L31.
- [3] G. Gisler, R. Weaver, C. Mader, M. Gittings, Two-and three-dimensional simulations of asteroid ocean impacts la-ur 02-66-30, *Science of Tsunami Hazards* 21 (2) (2003) 119.
- [4] K. A. Brakke, The surface evolver, *Experimental mathematics* 1 (2) (1992) 141–165.
- [5] C. Hirt, A. A. Amsden, J. Cook, An arbitrary Lagrangian-Eulerian computing method for all flow speeds, *Journal of Computational Physics* 14 (3) (1974) 227–253.
- [6] C. W. Hirt, B. D. Nichols, Volume of fluid (VOF) method for the dynamics of free boundaries, *Journal of Computational Physics* 39 (1) (1981) 201–225.
- [7] S. Osher, J. A. Sethian, Fronts propagating with curvature-dependent speed: algorithms based on hamilton-jacobi formulations, *Journal of Computational Physics* 79 (1) (1988) 12–49.
- [8] D. J. Benson, Volume of fluid interface reconstruction methods for multi-material problems, *Applied Mechanics Reviews* 55 (2) (2002) 151–165.
- [9] V. Dyadechko, M. Shashkov, Reconstruction of multi-material interfaces from moment data, *Journal of Computational Physics* 227 (11) (2008) 5361–5384.
- [10] K. So, X. Hu, N. Adams, Anti-diffusion interface sharpening technique for two-phase compressible flow simulations, *Journal of Computational Physics* 231 (11) (2012) 4304–4323.
- [11] X. Y. Hu, B. C. Khoo, An interface interaction method for compressible multifluids, *Journal of Computational Physics* 198 (1) (2004) 35–64.
- [12] S. Pan, X. Hu, N. A. Adams, High-resolution method for evolving complex interface networks, *Computer Physics Communications* , accepted.
- [13] D. P. Starinshak, S. Karni, P. L. Roe, A new level set model for multimaterial flows, *Journal of Computational Physics* 262 (2014) 1–16.
- [14] W. Zheng, J.-H. Yong, J.-C. Paul, Simulation of bubbles, *Graphical Models* 71 (6) (2009) 229–239.
- [15] R. P. Fedkiw, T. Aslam, B. Merriman, S. Osher, A non-oscillatory Eulerian approach to interfaces in multimaterial flows (the ghost fluid method), *Journal of Computational Physics* 152 (2) (1999) 457–492.
- [16] J. Wang, K. Liu, D. Zhang, An improved CE/SE scheme for multi-material elastic-plastic flows and its applications, *Computers & Fluids* 38 (3) (2009) 544–551.
- [17] E. Olsson, G. Kreiss, A conservative level set method for two phase flow, *Journal of Computational Physics* 210 (1) (2005) 225–246.
- [18] X. Hu, B. Khoo, N. A. Adams, F. Huang, A conservative interface method for compressible flows, *Journal of Computational Physics* 219 (2) (2006) 553–578.
- [19] M. Herrmann, A balanced force refined level set grid method for two-phase flows on unstructured flow solver grids, *Journal of Computational Physics* 227 (4) (2008) 2674–2706.
- [20] M. Herrmann, A parallel Eulerian interface tracking/Lagrangian point particle multi-scale coupling procedure, *Journal of Computational Physics* 229 (3) (2010) 745–759.
- [21] X. Hu, N. Adams, M. Herrmann, G. Iaccarino, Multi-scale modeling of compressible multi-fluid flows

- with conservative interface method, in: Proceedings of the Summer Program, Vol. 301, Center for Turbulence Research, 2010.
- [22] L. Han, X. Hu, N. A. Adams, Scale separation for multi-scale modeling of free-surface and two-phase flows with the conservative sharp interface method, *Journal of Computational Physics* 280 (2015) 387–403.
  - [23] J. Luo, X. Hu, N. Adams, Efficient formulation of scale separation for multi-scale modeling of interfacial flows, *Journal of Computational Physics* 308 (2016) 411–420.
  - [24] X. Hu, N. Adams, G. Iaccarino, On the HLLC Riemann solver for interface interaction in compressible multi-fluid flow, *Journal of Computational Physics* 228 (17) (2009) 6572–6589.
  - [25] L. Han, X. Hu, N. Adams, Adaptive multi-resolution method for compressible multi-phase flows with sharp interface model and pyramid data structure, *Journal of Computational Physics* 262 (2014) 131–152.
  - [26] B. Müller, F. Kummer, M. Oberlack, Y. Wang, Simple multidimensional integration of discontinuous functions with application to level set methods, *International Journal for Numerical Methods in Engineering* 92 (7) (2012) 637–651.
  - [27] S. Pan, X. Hu, N. Adams, A consistent analytical formulation for volume-estimation of geometries enclosed by implicitly defined surfaces, *arXiv preprint arXiv:1704.05355*.
  - [28] E. F. Toro, M. Spruce, W. Speares, Restoration of the contact surface in the hll-riemann solver, *Shock waves* 4 (1) (1994) 25–34.
  - [29] K.-M. Shyue, A fluid-mixture type algorithm for compressible multicomponent flow with mie-grüneisen equation of state, *Journal of Computational Physics* 171 (2) (2001) 678–707.
  - [30] V. Pasquariello, G. Hammerl, F. Örley, S. Hickel, C. Danowski, A. Popp, W. A. Wall, N. A. Adams, A cut-cell finite volume–finite element coupling approach for fluid–structure interaction in compressible flow, *Journal of Computational Physics* 307 (2016) 670–695.
  - [31] A. Harten, Multiresolution algorithms for the numerical solution of hyperbolic conservation laws, *Communications on Pure and Applied Mathematics* 48 (12) (1995) 1305–1342.
  - [32] O. Roussel, K. Schneider, A. Tsigulin, H. Bockhorn, A conservative fully adaptive multiresolution algorithm for parabolic pdes, *Journal of Computational Physics* 188 (2) (2003) 493–523.
  - [33] M. O. Domingues, S. M. Gomes, O. Roussel, K. Schneider, An adaptive multiresolution scheme with local time stepping for evolutionary PDEs, *Journal of Computational Physics* 227 (8) (2008) 3758–3780.
  - [34] S. Pan, X. Lyu, X. Y. Hu, N. A. Adams, High-order time-marching reinitialization for regional level-set functions, *Journal of Computational Physics* 354 (2018) 311–319.
  - [35] G.-S. Jiang, C.-W. Shu, Efficient implementation of weighted ENO schemes., *Tech. rep., DTIC Document* (1995).
  - [36] C.-W. Shu, S. Osher, Efficient implementation of essentially non-oscillatory shock-capturing schemes, *Journal of Computational Physics* 77 (2) (1988) 439–471.
  - [37] R. Saurel, R. Abgrall, A multiphase godunov method for compressible multifluid and multiphase flows, *Journal of Computational Physics* 150 (2) (1999) 425–467.

- [38] S. Galera, P.-H. Maire, J. Breil, A two-dimensional unstructured cell-centered multi-material ALE scheme using VOF interface reconstruction, *Journal of Computational Physics* 229 (16) (2010) 5755–5787.
- [39] X. Zeng, G. Scovazzi, A frame-invariant vector limiter for flux corrected nodal remap in arbitrary Lagrangian–Eulerian flow computations, *Journal of Computational Physics* 270 (2014) 753–783.
- [40] M. Kucharik, M. Shashkov, Conservative multi-material remap for staggered multi-material arbitrary Lagrangian–Eulerian methods, *Journal of Computational Physics* 258 (2014) 268–304.
- [41] D. P. Starinshak, J. Owen, A multimaterial extension to subzonal reconstruction, *Journal of Computational Physics* 313 (2016) 594–616.
- [42] V. A. Dobrev, T. E. Ellis, T. V. Kolev, R. N. Rieben, High-order curvilinear finite elements for axisymmetric Lagrangian hydrodynamics, *Computers & Fluids* 83 (2013) 58–69.
- [43] C. Joggerst, A. Nelson, P. Woodward, C. Lovekin, T. Masser, C. L. Fryer, P. Ramaprabhu, M. Francois, G. Rockefeller, Cross-code comparisons of mixing during the implosion of dense cylindrical and spherical shells, *Journal of Computational Physics* 275 (2014) 154–173.
- [44] D. Ranjan, J. Oakley, R. Bonazza, Shock-bubble interactions, *Annual Review of Fluid Mechanics* 43 (2011) 117–140.
- [45] A. Bagabir, D. Drikakis, Mach number effects on shock-bubble interaction, *Shock Waves* 11 (3) (2001) 209–218.
- [46] B. Hejazialhosseini, D. Rossinelli, M. Bergdorf, P. Koumoutsakos, High order finite volume methods on wavelet-adapted grids with local time-stepping on multicore architectures for the simulation of shock-bubble interactions, *Journal of Computational Physics* 229 (22) (2010) 8364–8383.
- [47] J.-F. Haas, B. Sturtevant, Interaction of weak shock waves with cylindrical and spherical gas inhomogeneities, *Journal of Fluid Mechanics* 181 (1987) 41–76.
- [48] R. R. Nourgaliev, T.-N. Dinh, T. G. Theofanous, Adaptive characteristics-based matching for compressible multifluid dynamics, *Journal of Computational Physics* 213 (2) (2006) 500–529.
- [49] J. H. Niederhaus, J. Greenough, J. Oakley, D. Ranjan, M. Anderson, R. Bonazza, A computational parameter study for the three-dimensional shock–bubble interaction, *Journal of Fluid Mechanics* 594 (2008) 85–124.
- [50] N. Zabusky, S. Zeng, Shock cavity implosion morphologies and vortical projectile generation in axisymmetric shock–spherical fast/slow bubble interactions, *Journal of Fluid Mechanics* 362 (1998) 327–346.
- [51] C.-H. Chang, X. Deng, T. G. Theofanous, Direct numerical simulation of interfacial instabilities: a consistent, conservative, all-speed, sharp-interface method, *Journal of Computational Physics* 242 (2013) 946–990.

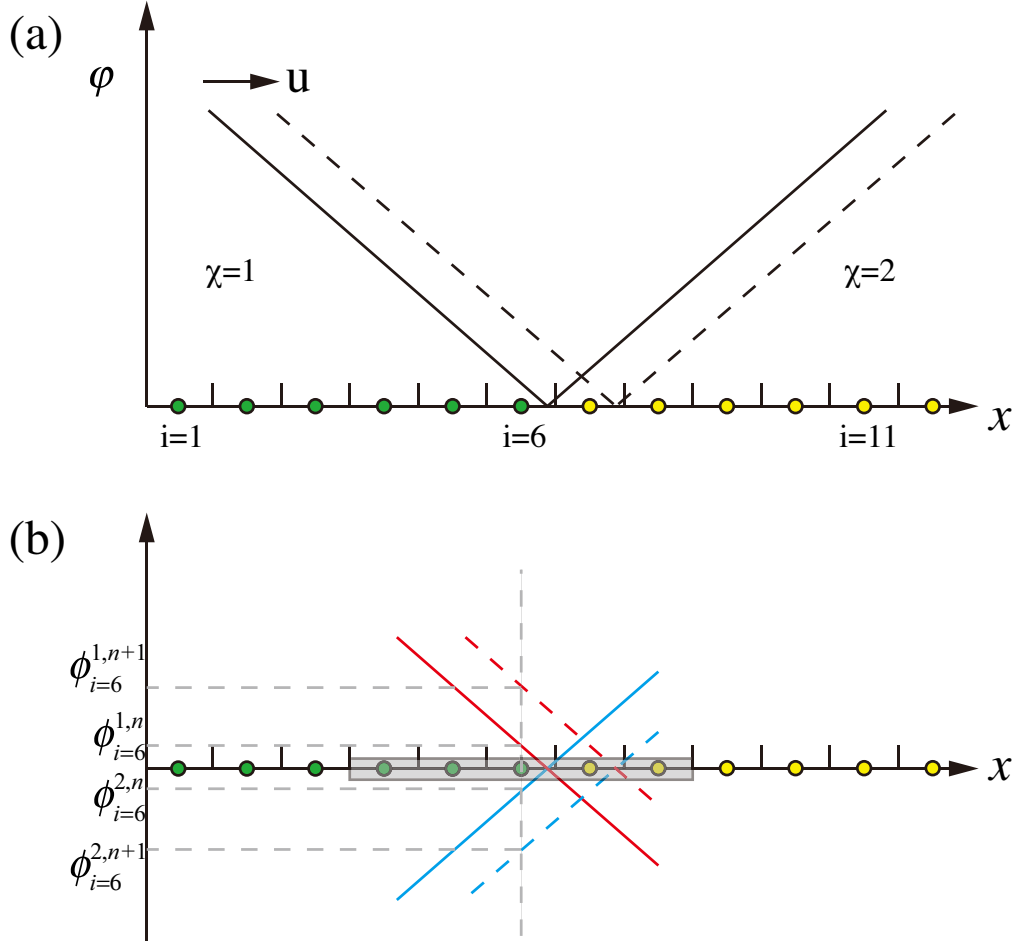


Figure 1: Schematic of the interface capturing method in Sec. 2.2 for a 1D two-region system. (a) The regional level-set function  $\phi^{\chi,n}$  at  $t^n$  is illustrated by the solid line. The dashed line indicates the exact  $\phi^{\chi,n+1}$  profile at  $t^{n+1}$  driven by a constant velocity  $u$ . (b) The local level-set functions  $\phi^{1,n}$  and  $\phi^{2,n}$  on the stencil (the gray box) of cell  $i=6$  are plotted by the blue solid line and the red solid line for the regions  $\chi=1$  and  $\chi=2$ , respectively. The corresponding evolved local level-set functions,  $\phi^{1,n+1}$  and  $\phi^{2,n+1}$ , are shown by the dashed lines.

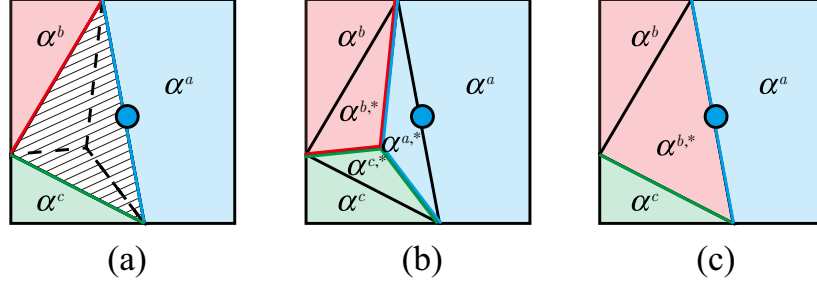


Figure 2: A schematic representation of volume fraction correction for a multi-material finite-volume cell to maintain conservation: (a) without modification, (b) sub-cell reconstruction and (c) conservation modification.

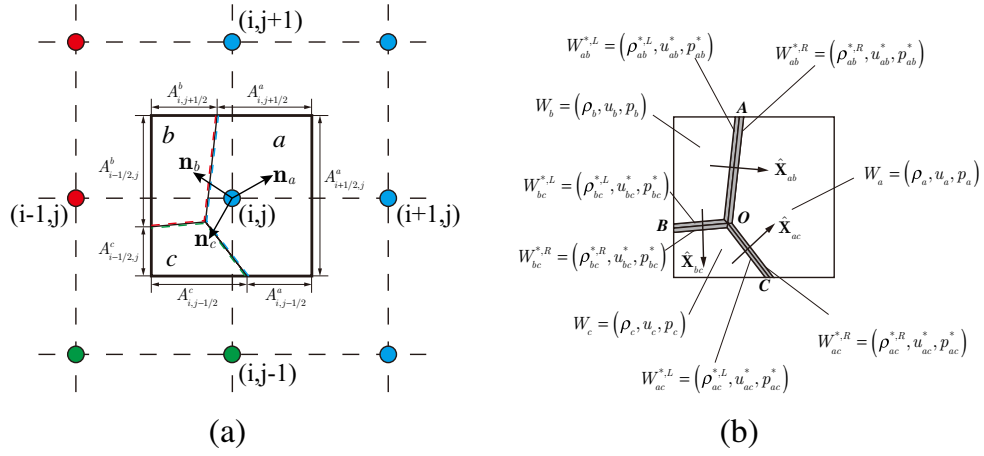


Figure 3: Schematic of conservative discretization for a 3-material cell.

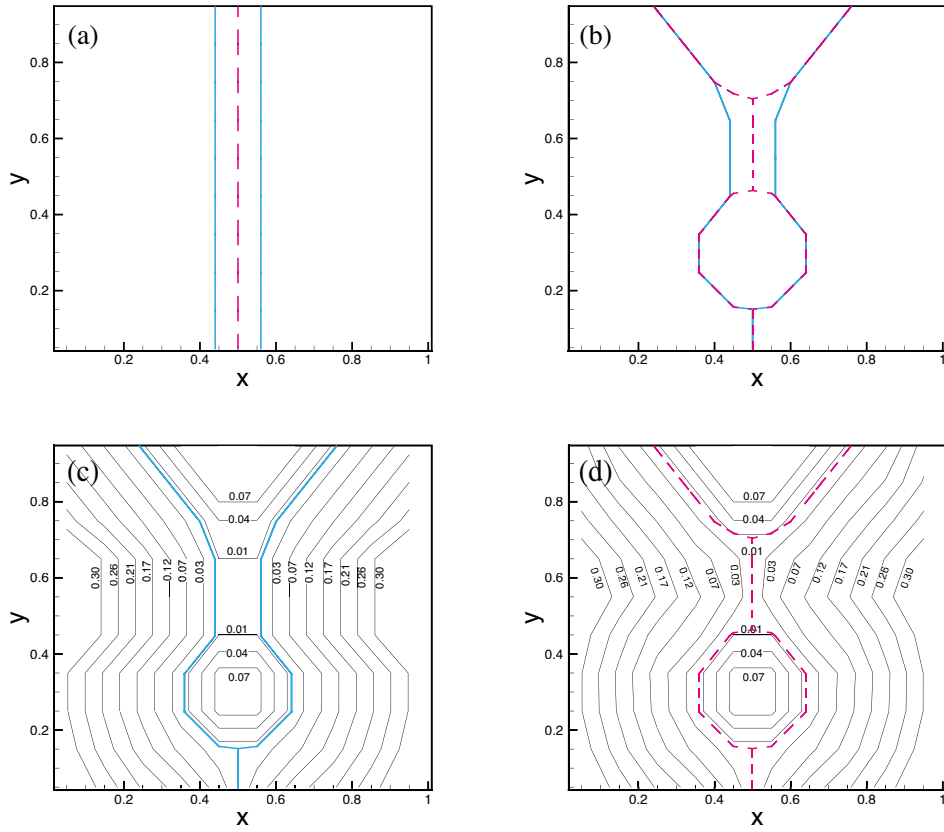


Figure 4: Simple test cases for multi-material interface scale separation model: (a) A thin filament and (b) a small droplet. The solid blue line and dashed red line indicate the interfaces before and after applying the scale separation model. (c) and (d) show the level-set contours before and after applying the scale separation model.

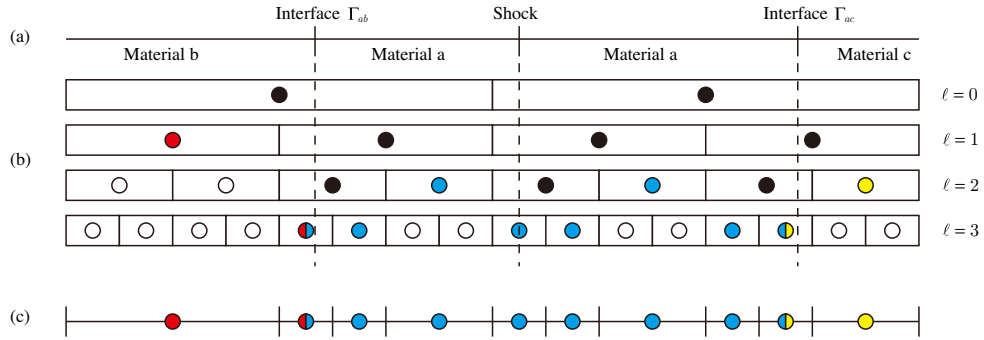


Figure 5: The multi-resolution representation of 3-material compressible flows in 1D. (a) The computational domain is partitioned by 3 materials ( $a$ ,  $b$ ,  $c$ ). Two interfaces  $\Gamma_{ab}$  and  $\Gamma_{ac}$  separate these materials, and a shock wave occurs inside material  $a$ . (b) The circles indicate the non-existing blocks. The black dots are the non-leaf blocks which have child blocks. The leaf blocks, colored by blue, red and yellow are blocks containing single material  $a$ ,  $b$  and  $c$ , respectively. (c) The final multi-resolution representation shows the single-material block of material  $b$  is located at the coarsest level as no shock wave or interface occur near it. The single-material block of material  $c$  is refined to  $\ell = 2$  because it is close to the interface  $\Gamma_{ac}$ . The single-material blocks of material  $a$  are either refined by interface or shock wave. All multi-material blocks are refined to the finest level.



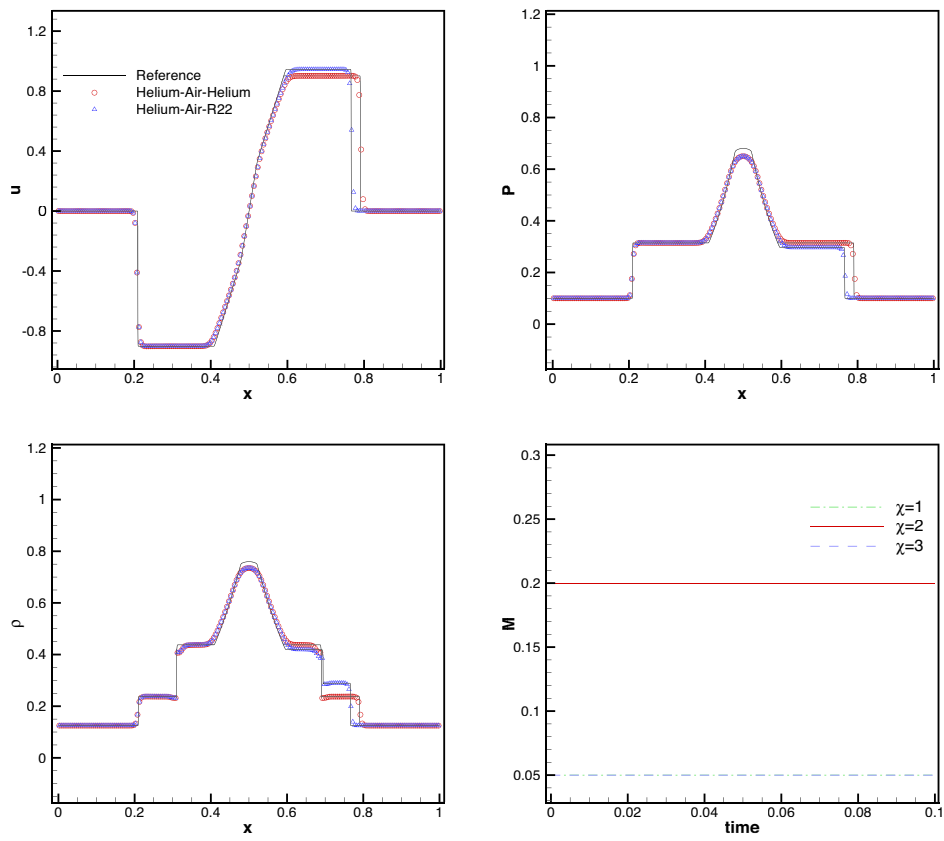


Figure 6: Three-material shock tube problem.

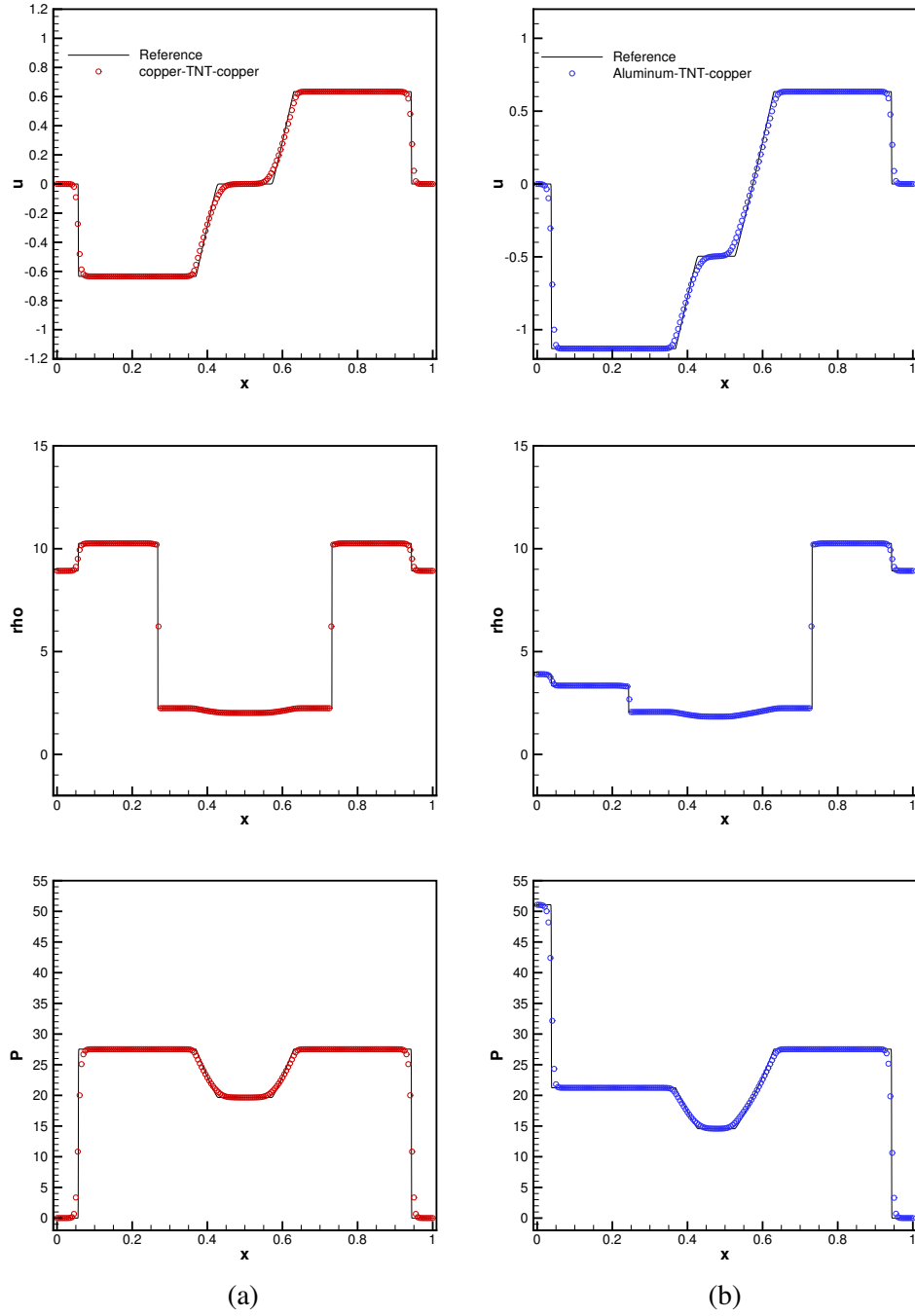
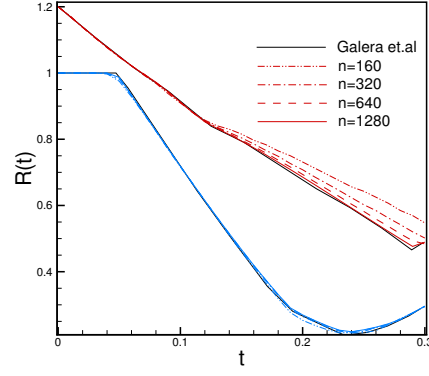
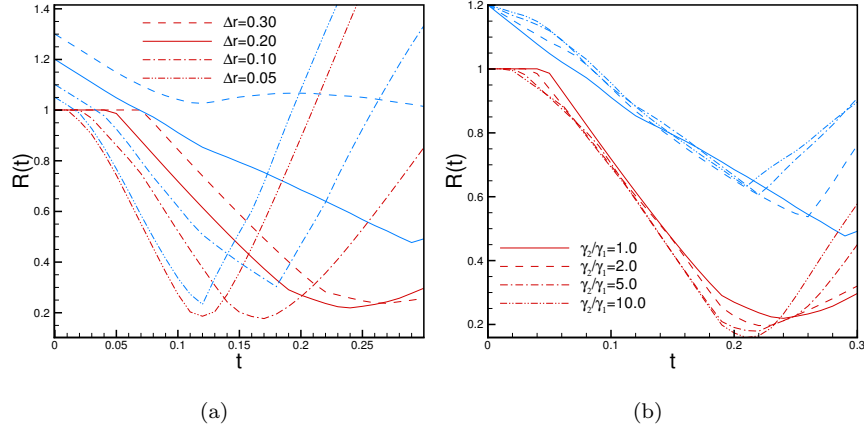


Figure 7: Three-material explosive driving and high-speed impact problems: (a) the copper-TNT-copper configuration and (b) the aluminum-TNT-copper configuration.



(a)

Figure 8: Trajectories of the inner (blue lines) and outer (red lines) interfaces of the shell in 1D ICF implosion problems.



(a)

(b)

Figure 9: Parameter study of the ICF implosion problem: (a) different shell thickness and (b) different  $\gamma_2/\gamma_1$ .

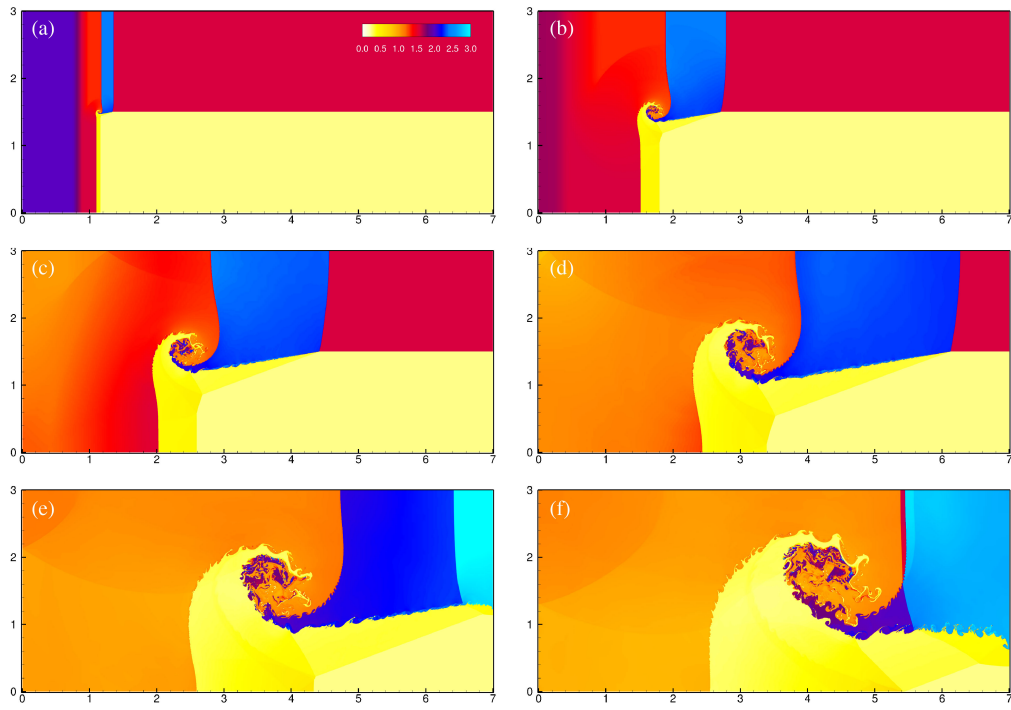


Figure 10: Internal energy distributions at  $t = 0.2, 1.0, 2.0, 3.0, 4.0$  and  $5.0$  for 2D compressible triple point problem with  $\ell = 5$ .

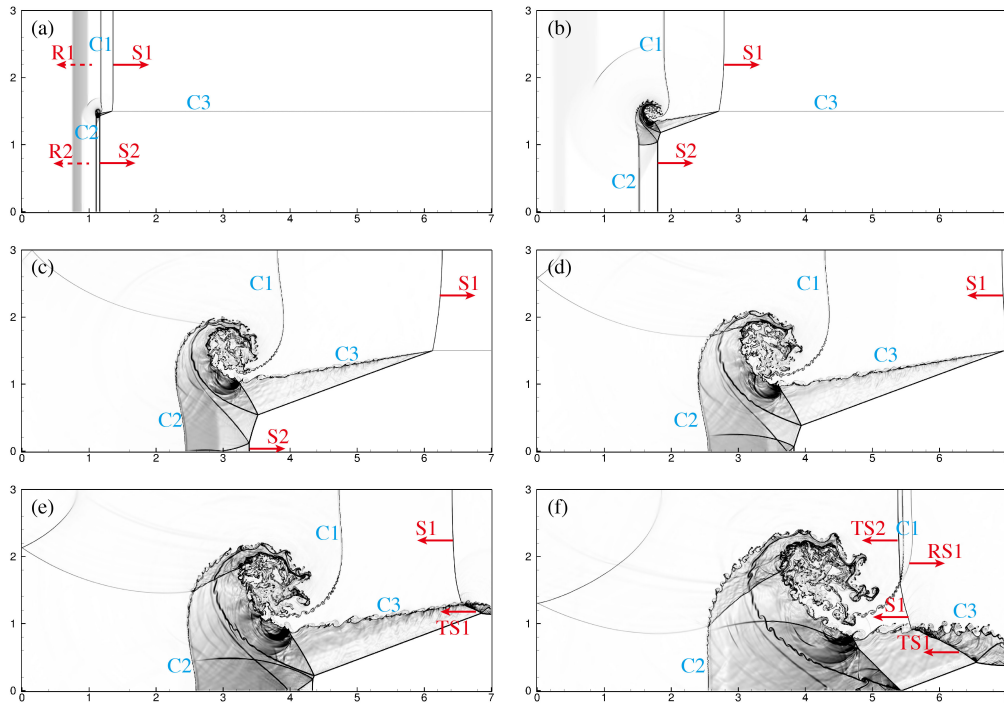


Figure 11: Snapshots of density gradient at  $t = 0.2, 1.0, 3.0, 3.5, 4.0$  and  $5.0$  for 2D compressible triple point problem with  $\ell = 5$ .

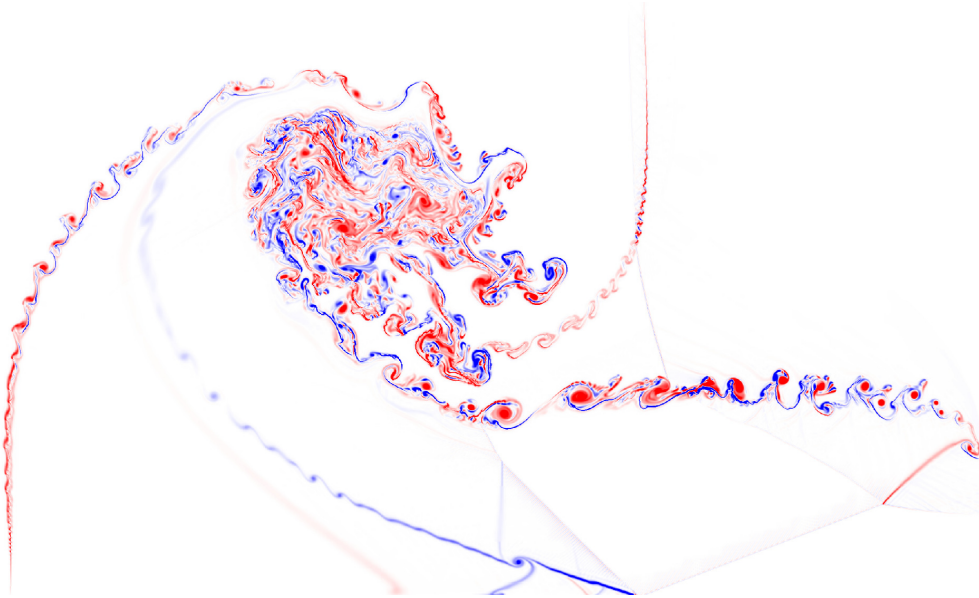


Figure 12: Vorticity contours at 5.0 for 2D compressible triple point problem with  $\ell = 5$ .

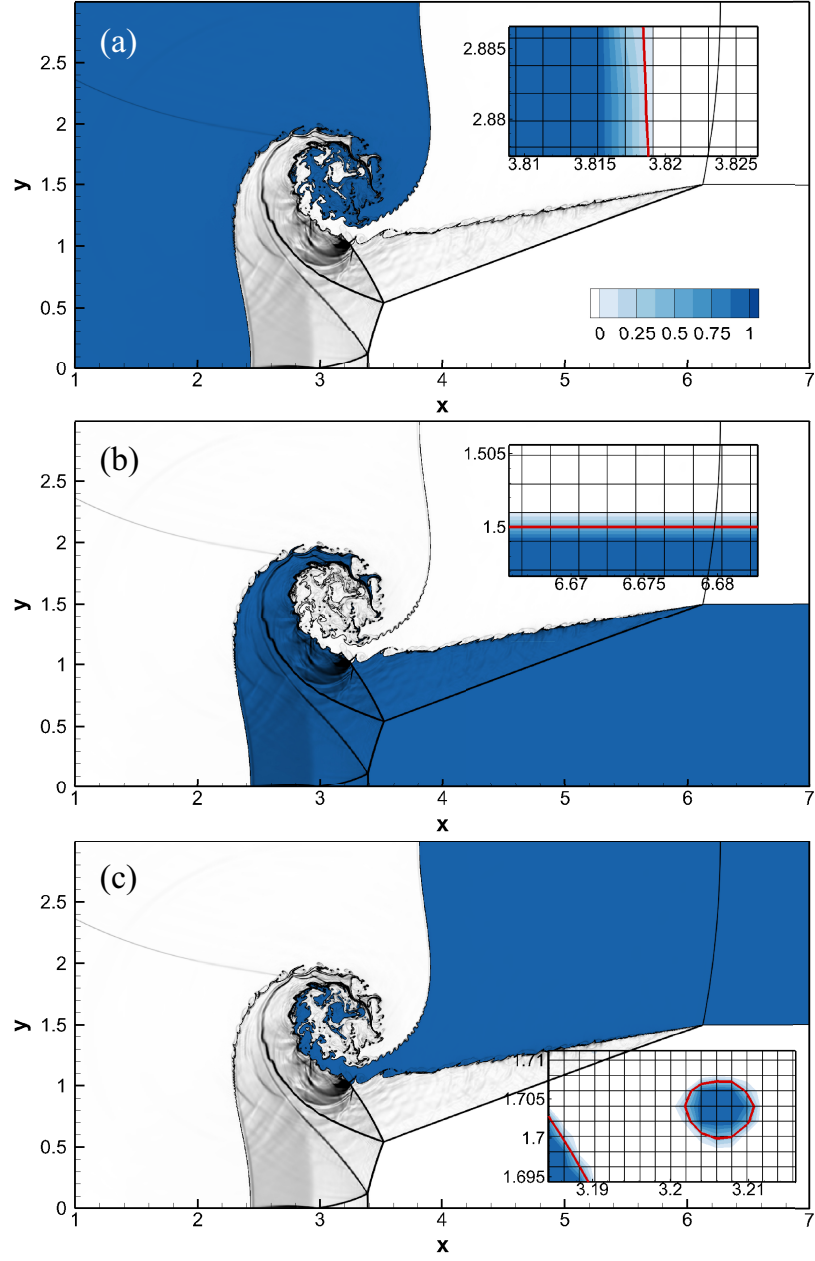


Figure 13: Volume fraction contours of  $\chi = 1$  (a),  $\chi = 2$  (b), and  $\chi = 3$  (c) at time  $t = 3.0$  for 2D compressible triple point problem with  $\ell = 5$ . The extracted interfaces (red lines) are shown in the insets.

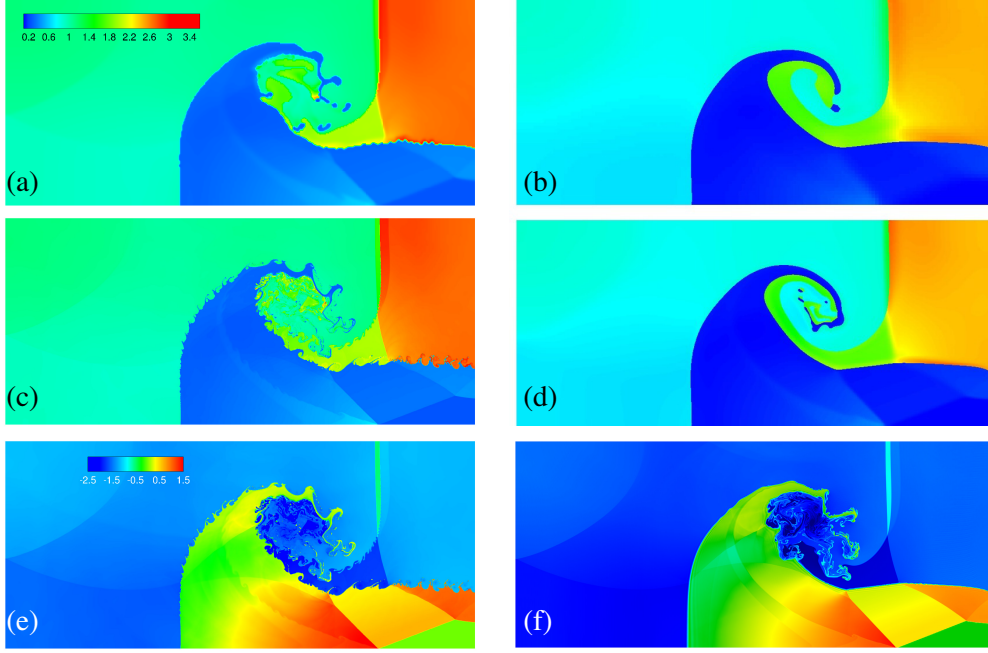


Figure 14: Comparison between the present numerical method (left column) and other existing methods [42, 41] (right column) for the 2D compressible triple point problem. The internal energy contours obtained by our numerical method with  $\ell = 2$  (an effective resolution of  $448 \times 192$ ) and  $\ell = 5$  (an effective resolution of  $3584 \times 1536$ ) are plotted in (a) and (c), respectively. The internal energy contours of the ALE method (reproduced from [41] with permission of Elsevier BV 2017) with resolution  $140 \times 60$  and  $560 \times 240$  are shown in (b) and (d), respectively. The density contours (logarithm scale) of our numerical method with  $\ell = 5$  and the curvilinear finite element method [42] (high-resolution results are available at <https://computation.llnl.gov/projects/blast/triple-point-shock-interaction>) are shown in (e) and (f), respectively.



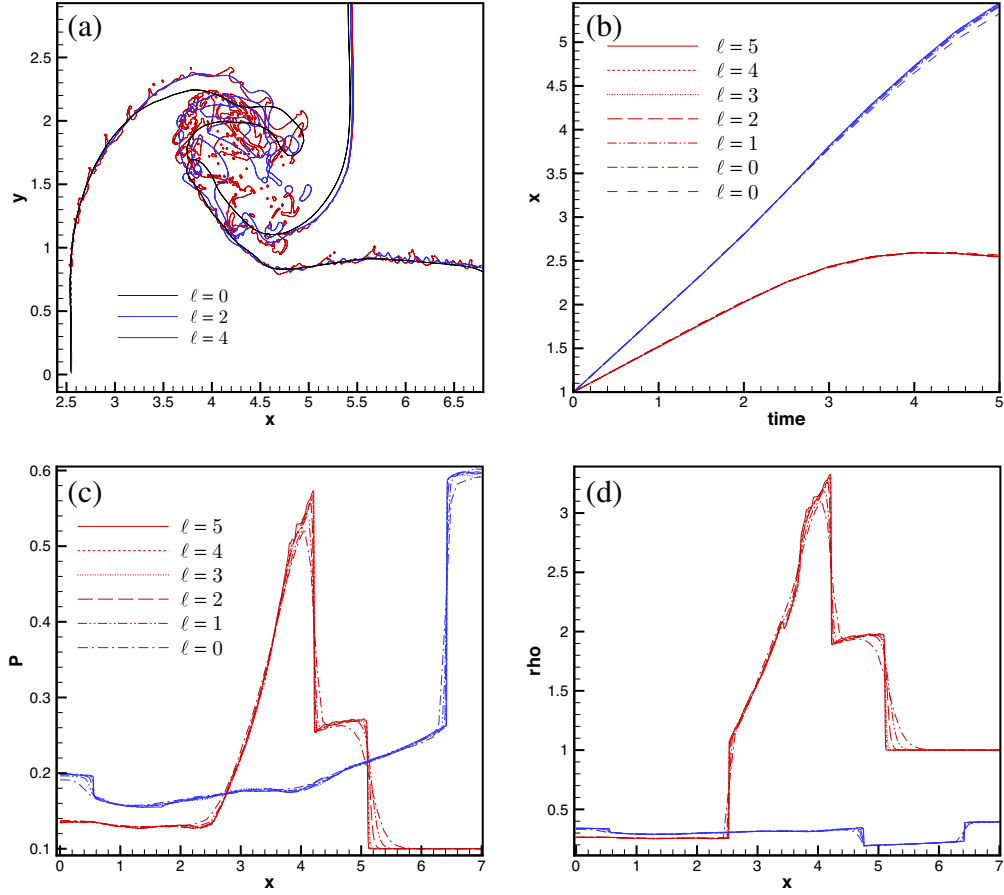


Figure 15: Grid convergence tests for 2D compressible triple point problem. (a) The interface networks at  $t = 5.0$  with different finest levels,  $\ell = 0$ ,  $\ell = 2$  and  $\ell = 4$ . (b) Convergence study of the interface location at the lower (red lines) and upper (blue lines) boundaries with increasing  $\ell$  from 0 (the second resolution with  $\ell = 0$  is half of the first one) to 5. The coarsest resolution is obtained with  $\ell = 0$  and the number of inner cells is 8 while in other simulations the number of inner cells is 16. (c) The pressure profiles along  $x$  direction at  $y = 0.5$  (red lines) and  $y = 2.5$  (blue lines) with  $t$  being 4.0.

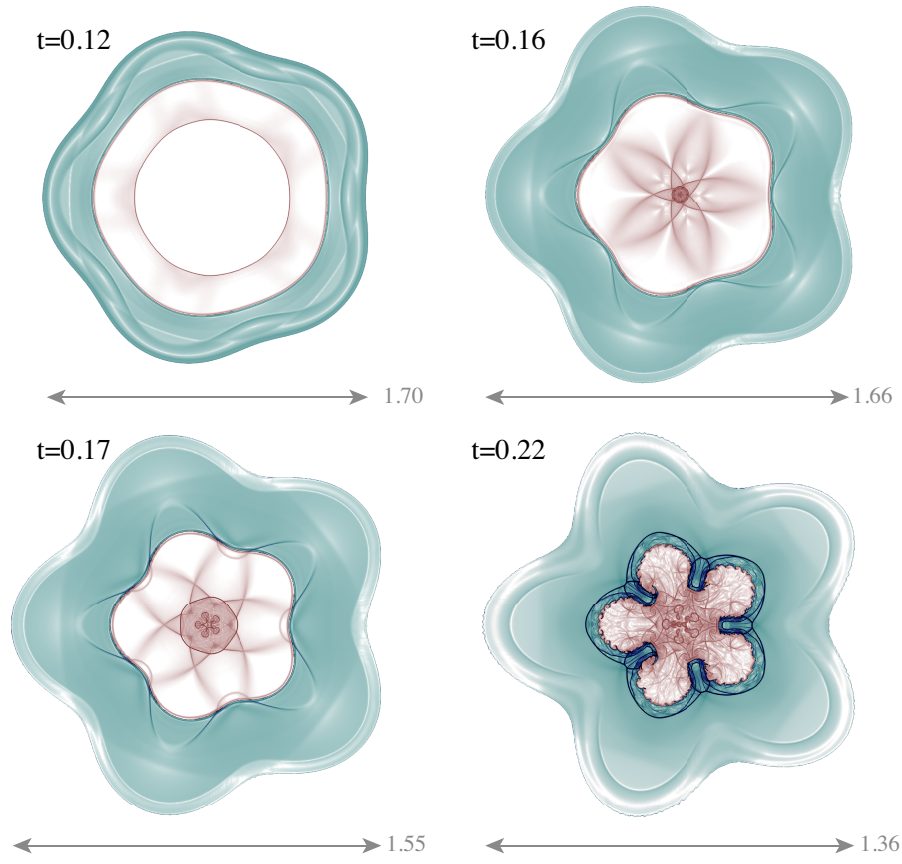


Figure 16: Snapshots of density gradient before the stagnation time for 2D cylindrical ICF implosion with a 5-mode perturbation.

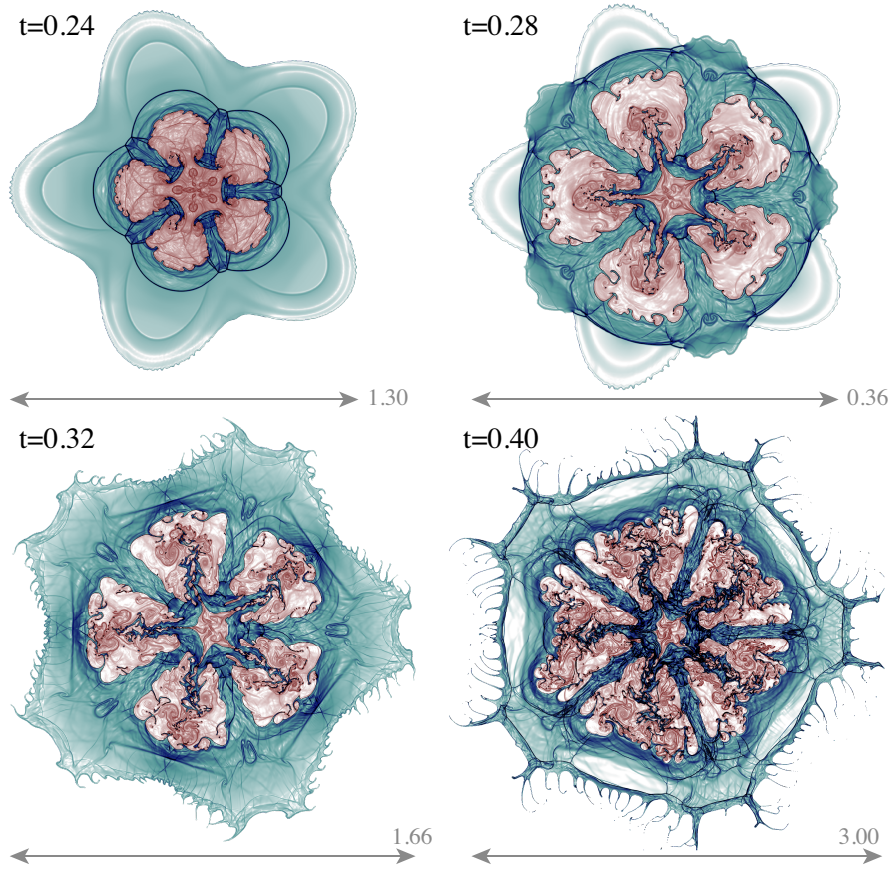


Figure 17: Snapshots of density gradient after the stagnation time for 2D cylindrical ICF implosion with a high-mode perturbation.

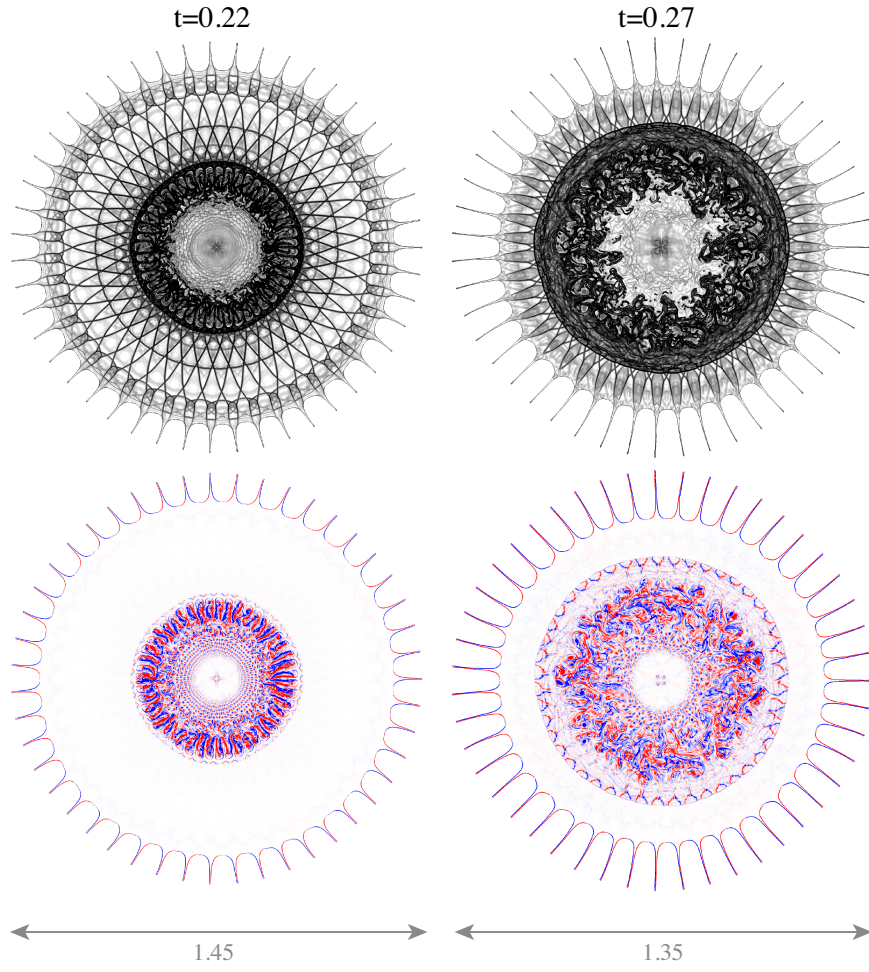


Figure 18: Snapshots of density gradient and vorticity at  $t = 0.22$  and  $0.27$  for 2D cylindrical ICF implosion with a high-mode perturbation.

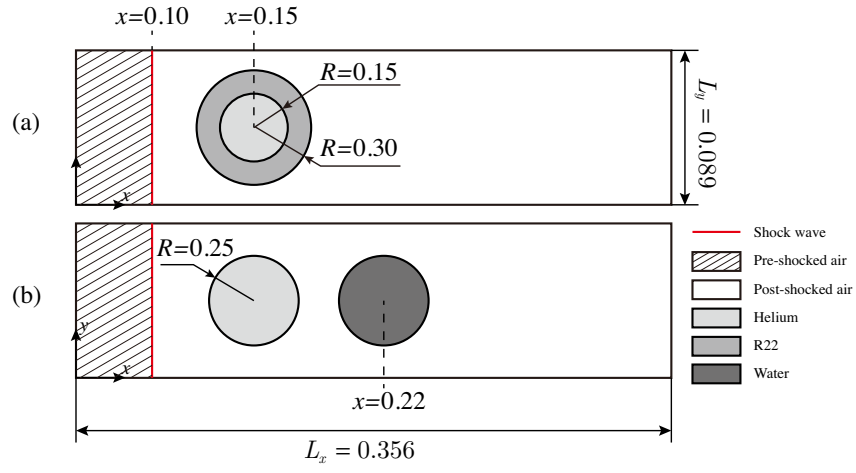


Figure 19: Computational domains for 2D compressible 3-material flows: (a) case V and (b) case VI.

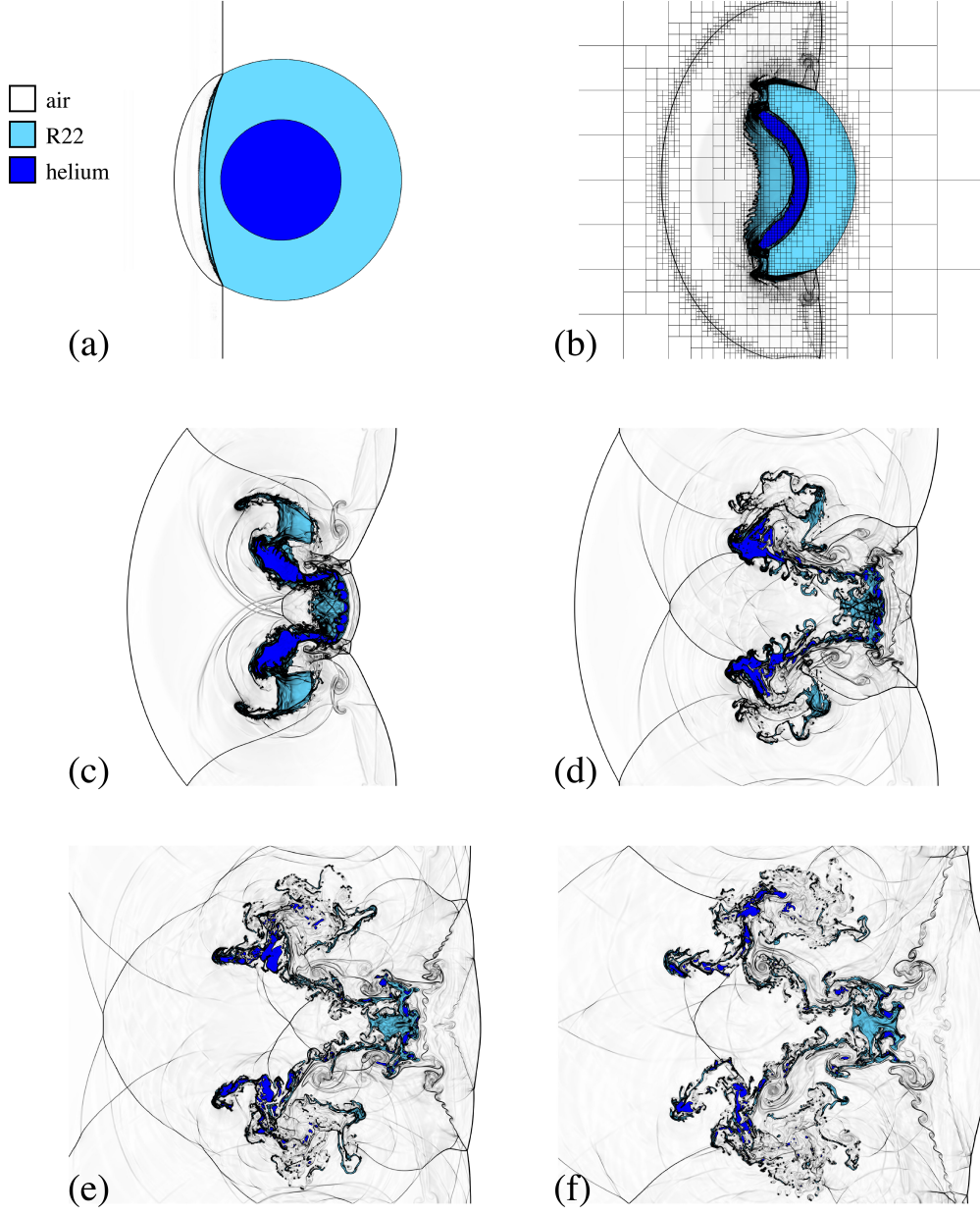


Figure 20: Density gradient fields and materials distribution of case V at (a)  $t = 5.0 \times 10^{-3}$ , (b)  $t = 1.0 \times 10^{-2}$ , (c)  $t = 1.5 \times 10^{-2}$ , (d)  $t = 2.0 \times 10^{-2}$ , (e)  $t = 2.5 \times 10^{-2}$  and (f)  $t = 3.0 \times 10^{-2}$ . A multi-resolution representation is outlined at  $t = 1.0 \times 10^{-2}$ .



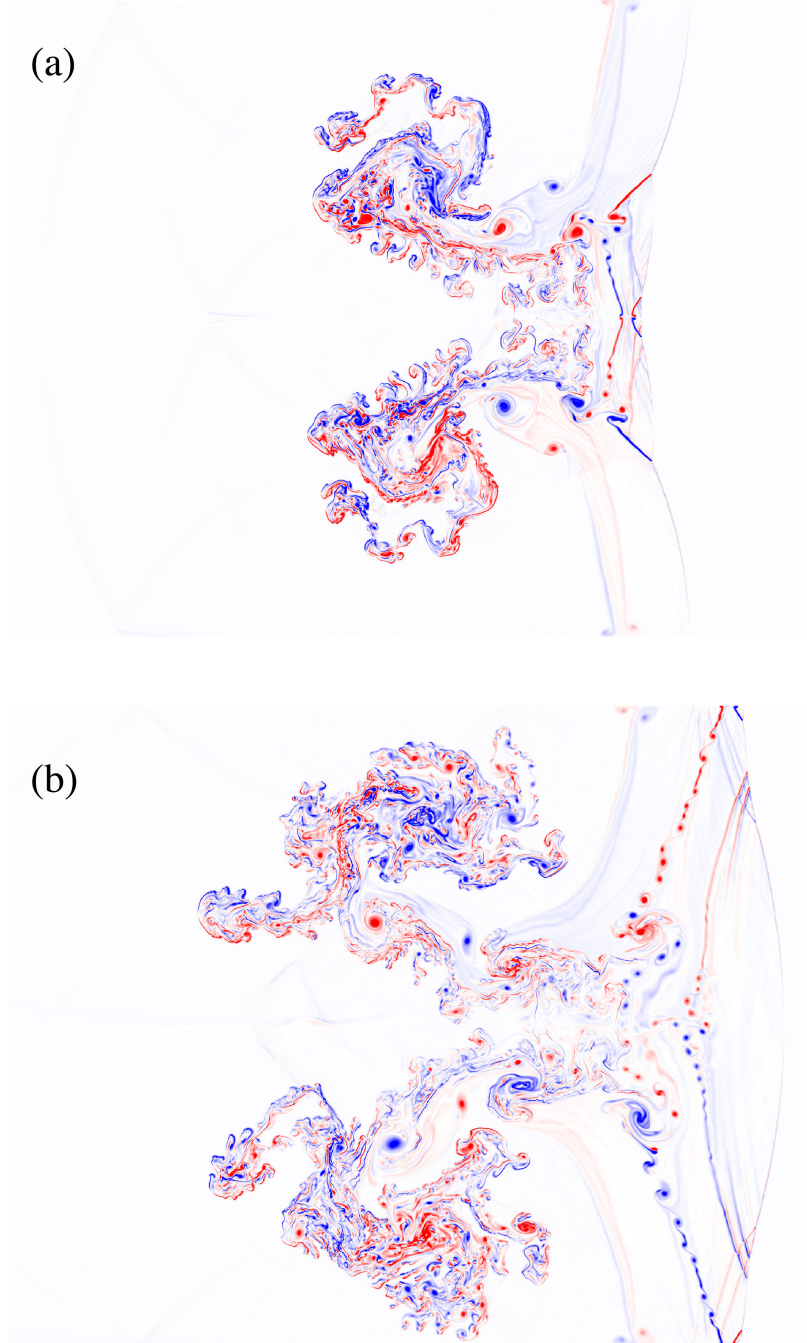


Figure 21: Vorticity contours of case V at (a)  $t = 2.0 \times 10^{-2}$  and (b)  $t = 3.0 \times 10^{-2}$ .

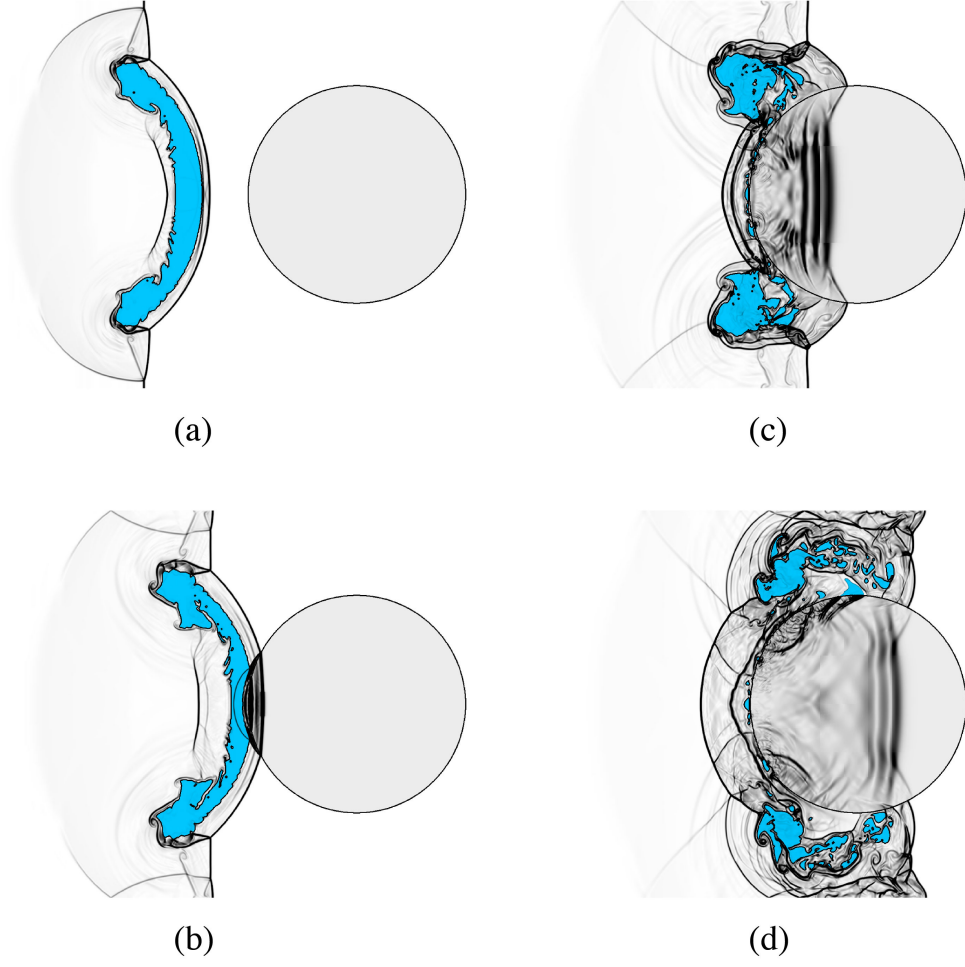


Figure 22: Density gradient fields of case VI at (a)  $t = 1.0 \times 10^{-2}$ , (b)  $t = 1.2 \times 10^{-2}$ , (c)  $t = 1.5 \times 10^{-2}$  na (d)  $t = 1.8 \times 10^{-2}$ . The distribution of helium is colored by blue to capture its interaction with water column (light gray).